Reviews of Modern Plasma Physics (2022) 6:32
https://doi.org/10.1007/s41614-022-00096-y

REVIEW PAPER

Dimensionality of solar magnetic reconnection

Jeongwoo Lee[1,2]

Received: 20 February 2022 / Accepted: 28 September 2022 / Published online: 19 October 2022

Abstract

Solar flares are the best examples of astrophysical magnetic reconnection in which the reconnection structure can be studied in detail. The structure is manifested through flare ribbons, intense optical and EUV emissions in footpoints of field lines attached to the coronal reconnection region. In the most common type of solar flares, two parallel ribbons appear and move away from each other, which could be related to the reconnection electric field under the theory of two-dimensional (2D) X-point reconnection, opening up a wide field of solar research. Another breakthrough came upon the discovery of circular ribbons, which implies a dome-shaped spine-fan structure capable of truly three dimensional (3D) null point reconnection. The variability of circular ribbons could also shed light on the reconnection electric field in the corona, but was relatively less attended. In this paper, we review selective topics in both types of flares with emphasis on the dimensionality of magnetic reconnection. Three types of reconnection: 2D X-point, 3D torsional, and 3D spine-fan reconnection are studied and associated with translational, rotational, and vibrational degrees of freedom. It is demonstrated that the dimensionality-based analysis of the observed dynamics of circular and parallel ribbons can facilitate a better understanding of the nature of solar magnetic reconnection.

Keywords Magnetohydrodynamics · Magnetic reconnection · Astrophysical plasmas · Solar magnetic fields · Solar flares

✉ Jeongwoo Lee
leej@njit.edu

[1] Institute for Space Weather Sciences and Center for Solar-Terrestrial Research, New Jersey Institute of Technology, University Heights, Newark, NJ 07102-1982, USA

[2] Big Bear Solar Observatory, New Jersey Institute of Technology, North Shore Lane, Big Bear City, CA 92314-9672, USA

1 Introduction

Dimensionality is an important ingredient in physics, as degrees of freedom, i.e., the maximum number of logically independent values, are set by the dimension of the system. In statistical mechanics, possible motions of particles are constrained by the dimension of the system, which leads to different thermodynamic properties like specific heat ratio and electronic susceptibilities (El-Batanouny 2020). Lattice dynamics also gives us properties such as thermodynamics, superconductivity, phase transitions, thermal conductivity, and thermal expansion (Hughes 1982). Likewise dynamical properties of fluids change depending on the dimension of the system so that dimensional analysis allows exploration of both the laminar and turbulent limits and understanding of basic physics in fluid motion (Jensen 2013).

Dimensionality is evidently important in magnetic reconnection too, as it limits the degrees of freedom available to the motion of interacting magnetic fields in the system. The concept of magnetic reconnection was introduced by Dungey (1961) to model the Earth's open magnetosphere. Ever since Sweet (1958) and Parker (1957) presented a two dimensional (2D) model, in which a current sheet stretches along the boundary between oppositely directed magnetic fields, the resulting rate of reconnection has always been calculated to be too slow to explain the explosive energy release during a solar flare. Petschek (1964) presented another framework in which the central current sheet is small and much less elongated, and this mechanism does operate fast enough to explain a flare that proceeds at typically a tenth or a hundredth of the Alfvén speed. Efforts to prove the highly efficient reconnection in astrophysical settings has been made in laboratory experiments without full success yet (Yamada et al. 2004). Three-dimensional (3D) reconnection theory came up much later to demonstrate that 3D reconnection is significantly different from that in 2D (Schindler et al. 1988; Hornig and Schindler 1996; Hornig 2001, 2007). For the latest progress in 3D magnetic reconnection, we refer to the reviews by Li et al. (2021) and Pontin and Priest (2022).

Magnetic reconnection in the sun, like in any astrophysical settings, has to rely on remote observations, and the information that we can get from the sun may not be the same as those obtained by in-situ observations (Paschmann et al. 2013) and also different from laboratory physics (Yamada et al. 2004). Solar magnetic field lines are anchored in the photosphere (Priest 2014), and we can observe bright emissions in the footpoints of the field lines attached to the coronal reconnection region. As magnetic energy is released via reconnection, it is used to accelerate charged particles in the corona, which then precipitate down to the solar atmosphere along the field lines to interact with cold plasma in the chromosphere and photosphere to subsequently heat them. Heated plasma in the solar atmosphere produces bright emissions in (E)UV and optical wavelengths called flare ribbons, and their morphology has provided clues to the physical process in the coronal magnetic reconnection (Zirin 1988; Longcope 2020). As the flare ribbons are projection of the coronal region onto the surface, 2D ribbon structure may represent 3D coronal reconnection structure, and 1D ribbon structure can tell 2D coronal reconnection, while no reconnection is possible in 1D.

Most widely studied flare ribbons are so-called two parallel ribbons (PRs), which appear on both sides of magnetic polarization inversion line (PIL), and separate away from each other during solar flares (e.g., Kopp and Pneuman 1976). Observed phenomenology of the parallel ribbon flares (PRFs) could be understood in terms of a simple 2D framework with an X-point configuration to provide a handy method for measuring a reconnection rate directly from the local speed and magnetic field at the flare ribbons (e.g., Forbes and Priest 1984; Forbes and Lin 2000; Priest and Forbes 2000). This procedure became so routine in studies of PRFs to bring up an extensive volume of research on solar magnetic reconnection in many decades. Eventually a group of scientists, Carmichael (1964), Sturrock (1967), Hirayama (1974) and Kopp and Pneuman (1976), established the 2D standard model for solar eruptive flares, also called CSHKP model, which provides a unified framework for direct measurement of the coronal reconnection rate from observables as well as explaining many observed behaviors.

Anomalous behaviors of PRs that are not directly addressed by the standard 2D model are also found. Those phenomena include nonuniform structure of brightness and speed along the ribbon axis (Asai et al. 2004; Jing et al. 2007; Liu et al. 2008), distinct morphology of Hα ribbons and hard X-ray sources (Asai et al. 2004; Liu et al. 2007), stepwise ribbon motions and variability of ribbon area (Lee et al. 2006), and discrete fine structures inside ribbons (Jing et al. 2016; Wyper and Pontin 2021). These issues could be addressed by extending the 2D model to include the other dimension yet keeping the X-point reconnection physics. Some studies utilized particle-in-cell (PIC) simulation to explore microphysics in the scale of the current sheet (Zhang et al. 2021; Guo et al. 2015, 2021). In particular, Zhang et al. (2021) investigated how particle acceleration rate depends on magnetic shear, which indirectly demonstrates the influence of the dimensionality on the reconnection efficiency.

Another type of solar flares called circular ribbon (CR) flares (CRFs) was found. Unlike PRF studies, CRF studies came with significant magnetohydrodynamics (MHD) simulation. Early comprehensive studies of CRFs were presented by Masson et al. (2009) and Reid et al. (2012) for a confined flare using 1600 Å ultraviolet images from TRACE to identify a line-tied fan-spine structure with the most representative structure for CRFs. Wang and Liu (2012) studied a set of CRFs, and asymmetric CR motions along with homologous jets using classical Hα data of Big Bear Solar Observatory (Zirin 1988).

Studies of CRFs mainly adopted 3D MHD simulation as a tool for physical interpretation, as an analytical approach seems not promising. Masson et al. (2009) and Reid et al. (2012) suggested that the singular spine field lines could be embedded in a somewhat larger quasi-separatrix layer (QSL) structure. The outer spine field can connect back to the surface to produce remote brightenings, but can also be open to generate jets (Pariat et al. 2009, 2010). A resistive MHD simulation for spine-fan reconnection found that the footpoint locations of field lines initially lying under the dome end up outside the dome after the reconnection and those beginning outside the dome end up inside (Pontin et al. 2013). Elongated outer ribbons appear to be related to the squashing factor (Titov et al. 2002), which indicates strong gradients of the field line mapping (Pontin et al. 2016). The finite cross section of a QSL also

seems consistent with the observed elongated spine-related ribbons (Masson et al. 2017).

Reconnection of field lines within QSLs shows up in the observations as a phenomenon known as slipping reconnection (Aulanier et al. 2006). The footpoints of the reconnecting field lines, and correspondingly, the precipitation sites, apparently slip through the plasma at a potentially high apparent speed along the chromospheric intersection of the embedding QSL. This includes so-called slip-running reconnection, where the slipping is super-Alfvénic (see, for example, Dudík et al. 2014, 2016). Masson et al. (2009) and Reid et al. (2012) showed that after the reconnection at the null point, the slipping motion is away from the null point and the initial location of the outer spine, which accounts for the successive brightening of the CR. Transformation of a CRF to a TRF has also been reported (Zhong et al. 2019), and two different types of confined flares are suggested based on the role of filament and the nonpotentiality of the ambient magnetic field (Li et al. 2019). These works highlight the complexity in triggering reconnection in spine-fan structures.

In this paper, we study the physical nature of solar flares from the viewpoint of the dimensionality of magnetic reconnection. Since theoretical properties of the 2D and the 3D reconnection physics are well documented elsewhere (Priest and Pontin 2009; Pontin 2011, 2012; Pontin and Priest 2022), we focus on their application to solar observations. In Sect. 2, we introduce solar flare phenomenology and state the dimensionality problem. In Sect. 3 we briefly review basic requirement for 3D reconnection, and formulate reconnection rates and energy conversion rates, which allows fast comparison of such theories with solar observations. In Sect. 4, we present solar observations that can evidence theoretical 3D reconnection. In particular, we relate the observed behaviors of CRFs to the modes of kinematic reconnection. In Sect. 5, we discuss solar magnetic reconnection in a magnetic arcade structure, and demonstrate anomalous behaviors of PRFs which do not fit to the standard 2D model. Finally, we summarize the lessons learned from this study in a way to contrast the 2D and 3D reconnection in solar flares and discuss future perspectives in Sect. 6.

2 Dimensionality in solar flare phenomenology

We introduce commonly-used solar flare terminology using Fig. 1. A theoretical spine and fan field structure is shown in Fig. 1A, B, where the spine fields coming toward the null point (black dot in the middle) diverge out to infinity on the xy-plane to form the fan surface. In the sun, however, we can see only the field lines rooted in the surface either by one foot or both. We therefore need to bend the fan field lines down to the photosphere as shown in Fig. 1B so that those fan field lines form the circular footpoints (CR) encircling the spine footpoint (IR). We thus end up with a single polarity region surrounded by a dome-shaped fan surface in the other polarity as shown in Fig. 1C.

Further complications in the real world are introduced in Fig. 1a–g. In panels (a, b) the dark feature is the QSL, as visualized by using high squashing factor, $\log Q$, which indicates strong gradients of the field line mapping (Titov et al. 2002). More advanced

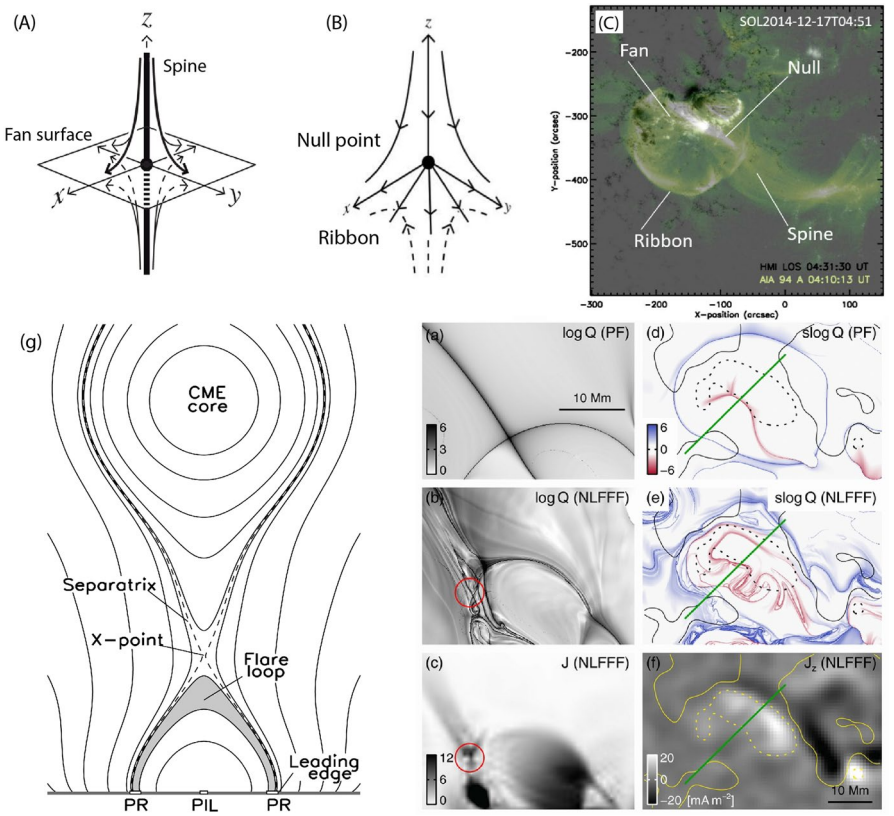

Fig. 1 CRF and TRF. The fan surface in the 3D null structure (**A**) should be bent down to make its outskirts a CR (**B**) in the photosphere (Source: Priest 2014). **C** An EUV image of the SOL2014-12-17T04:51 flare shows a circular dome shape (Source: Lee et al. 2020a). **a**–**f** Maps of squashing factor and current density clearly reveal the separatrices around the 2011-11-15 CRF (Source: Sun et al. 2013). **g** The geometry of the 2D standard flare model. Solid lines represent magnetic fields and the dashed line is the separatrix, which also defines the X-point

is the signed squashing factor, $s \log Q$, shown in panels (d, e). The QSLs in panel (a, d) manifest the fan and inner/outer spine as well as the null point in the potential field (PF) model. Those in panels (b, e) show the same in the nonlinear force free field (NLFFF) model, which is believed to represent the real coronal field more closely. Panels (c, f) are the corresponding current density maps obtained from the NLFFF model. Figure 1g shows the standard model for eruptive solar flares, in which the X-point is located above the closed flare loop and below an erupting filament called a coronal mass ejection (CME).

Obviously, all solar flares occur in 3D, and yet we are eager to find cases that can be approximated by a 2D framework because 2D theory offers a simple and clear interpretation of magnetic reconnection. Figure 2 is meant to make an argument as to why 3D theory is needed for some types of solar flare, but not others. Top panels are two Hα images selected for contrasting ribbon symmetry, and the bottom panels are skeleton

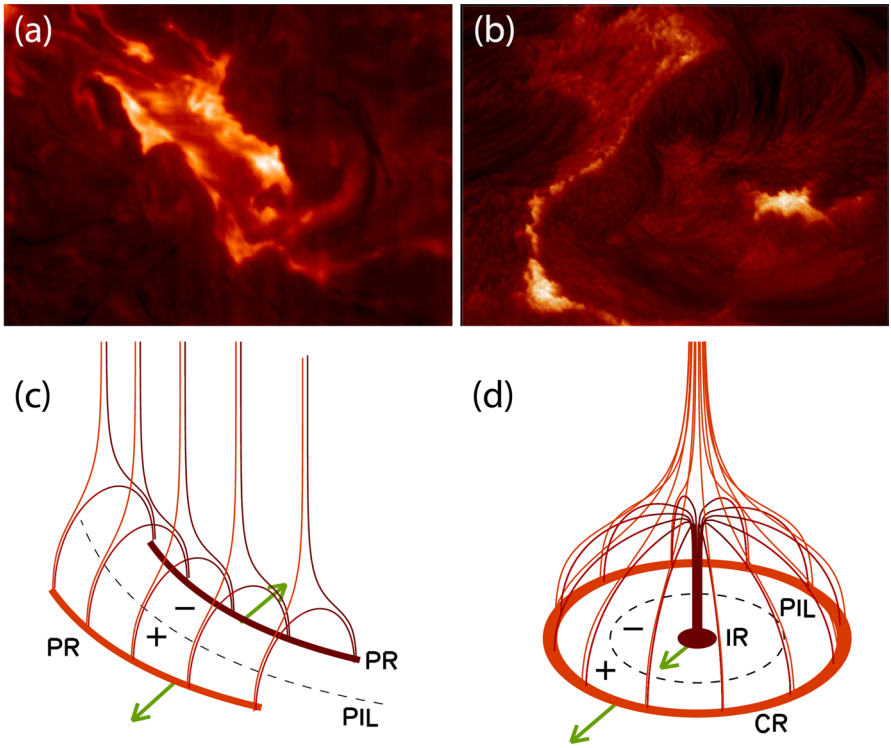

Fig. 2 Two types of Hα flare ribbons: **a** two PRs observed during the 2003-10-13 PRF (credit: Astronomical Institute, University of Wroclaw, Poland) and **b** highly asymmetric ribbons during the 2010-11-06 CRF (credit: Kuridze et al. 2013). Schematic skeleton representation of the PRF with an arcade of 2D field lines (**c**) and that of the CRF with a spine-fan structure (**d**). Note the difference between the ribbon motions (green arrows) relative to the PIL (dashed lines)

models. Theoretically we may imagine a limiting case that ribbons (Fig. 2a) become so highly asymmetric that one shrinks to a point, while the other completely surrounds it so as to make a CRF (Fig. 2b). Panels (c) and (d) show such a transformation of two ribbons into an inner ribbon (IR) and an outer ribbon (CR).

In observations CR often moves away from the PIL, which can be regarded as a process of sucking up more flux to fuel the reconnection. Then the reaction of IR to the expansion of the CR, should shrink to a point. Not only is this physically impossible but solar observations show that both IR and CR increase in size during flares. Explanation of IR expansion in the traditional paradigm needs an inward moving CR front, and the coronal reconnection point should also move to the center of CR and IR circles. The sun does not seem to support this scenario. This means that a CRF may not be understood as a variant of a PRF formed by rolling up a linear ribbon to meet end to end. It turns out, however, that the properties can be explained by the behavior of the current configuration around the 3D null point. This example demonstrates that not every type of solar flare can be cast into the 2D picture. Understanding of a CRF phenomenology needs a fully 3D magnetic reconnection model.

3 Magnetic reconnection theory

To facilitate physics-based discussion on the dimensionality of solar magnetic reconnection, we briefly check theoretical concepts and basic formulations. Our goal is not to present a complete review of theory but to discuss why such theoretical concepts are also needed for solar study, and what can be tested against solar observations. In this effort, we briefly review how 2D and 3D reconnection are distinguished in theory, and attempt to formulate the magnetic reconnection rates and energy conversion rates in terms of solar observables.

3.1 Distinction between 2D and 3D reconnection

There are several ways to explain how 3D reconnection differs from 2D reconnection. We review three of them and provide insights from solar physics perspectives.

3.1.1 Flux-conserving velocity

The formal proof of the 2D and 3D reconnection can be made in terms of the continuity equation for magnetic field and a flux-conserving velocity $\mathbf{w}$ (Schindler et al. 1988; Hornig and Schindler 1996; Hornig 2007, 2001; Priest et al. 2003):

$$\frac{\partial \mathbf{B}}{\partial t} - \nabla \times (\mathbf{w} \times \mathbf{B}) = 0. \tag{1}$$

In the 2D reconnection, the solution for $\mathbf{w}$ exists and is smooth and continuous everywhere except X-points where it is singular. Therefore, the field lines evolve as if they are reconnected at this point only, and the reconnection of magnetic field lines occurs in a one-to-one pairwise fashion at a single point. However, in the 3D reconnection, no solution for $\mathbf{w}$ exists for the flow threading the diffusion region. For a proof, we refer to Priest et al. (2003). As a result, magnetic field lines are not reconnected in a one-to-one fashion. Consequently 3D reconnection exhibits many distinct properties that are not shared by 2D reconnection [see, for further discussion, Pontin (2012), Priest et al. (2003)].

An observational test of this theory may be checking whether or not we can trace flare kernel pairs engaged in a single isolated event of reconnection. Observations of UV flare kernels would make a suitable dataset for this study as we can count pairs of the kernels in both magnetic polarity regions (Fletcher et al. 2004; Naus et al. 2022). Imbalance in the number and magnetic flux of kernels in either side of footpoints or disordered motions of kernels often found in solar observations might represent an intrinsic nature of 3D reconnection, not necessarily any limitation of observational capability.

3.1.2 Topological changes

A more clear demonstration of the issue of traceability of the field line connectivity in 3D reconnection was presented by Pontin (2011) as reproduced in Fig. 3. Here two colored flux tubes come to the diffusion region (shaded gray-scale surfaces) to reconnect. The colored bands are used as identifiers of the magnetic connectivity just like a rubber band for a pencil grip is used as a pencil identifier. The tube denoted A was initially connected to be B (Fig. 3a). Suppose, upon the interaction of the two flux tubes in the diffusion region (Fig. 3b), A is connected to D. If this means that B is connected to C, then such interaction is called 2D reconnection. Namely, in 2D reconnection, A (B) remains to be A (B), which is also indicated by the green bands. Same for the C and D as indicated by the black bands. It does not matter whether or not flux tubes have finite volumes in the 3D space.

Pontin (2011) demonstrated, based on the steady-state kinematic solution of Hornig and Priest (2003), that this is not the case in the 3D reconnection (Fig. 3d–f). Again, there are two field lines about to enter the diffusion region. One of them connects plasma elements labeled A and B, while the other connects plasma elements C and D. If the field lines are chosen such that after reconnection A is connected to C, then B will not be connected to D. This is shown graphically such that initially single colored flux tubes (Fig. 3d) split themselves passing through the diffusion region (Fig. 3e) and appear in mixed colors after the reconnection (Fig. 3f). In this case,

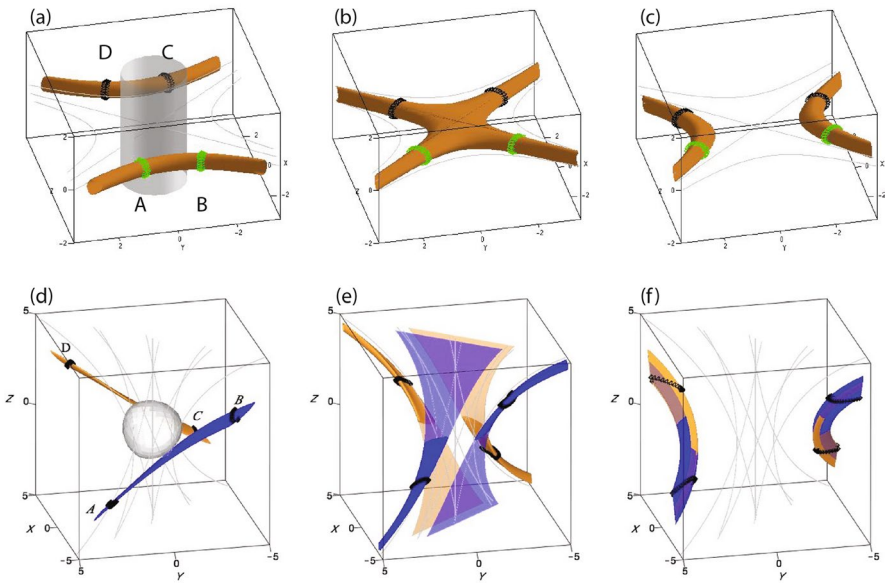

Fig. 3 Illustration of the 2D and the 3D reconnection. In the 2D reconnection, change of the connectivity of two interacting flux tubes (marked by colored grip bands) can be traced on a one-to-one basis (**a**–**c**). In the 3D reconnection, two flux tubes (marked by black bands) should be traced in a different way as indicated by the transparent sections during the reconnection and the mixed colors in each tube after the reconnection (**d**–**f**). A local non-ideal region is plotted as a gray volume around the X-point (**a**) and a 3D null-point (**d**). Source: Pontin (2011)

the bands are plotted with no distinct colors, and the identifier notations, A–D, are no longer used after the reconnection. In short, if the change of connectivity can be traced on a one-to-one basis, it is defined as 2D reconnection and otherwise 3D reconnection.

To this proof, we want to add a phenomenological interpretation of magnetic reconnection using an analogy with the lattice dynamics. In Fig. 3a–c, the connectivity change from A–B to C–D occurred via translational motion only, regardless of the finite thickness of the flux tubes or possibly uneven shapes. On the other hand, the rotational motion of the tubes around the diffusion region is introduced in the 3D reconnection (Fig. 3e–f), which is analogous to the difference between 1D and 2D/3D lattice dynamics. Another possible degree of freedom is the vibrational motion, which is likely to be associated with magnetic shear motion. What makes 3D reconnection different may be the rotational and vibrational degrees of freedom in the motions around the 3D null point.

3.1.3 Non-zero $\mathbf{E} \cdot \mathbf{B}$

We can distinguish 2D from 3D reconnection by checking whether or not $\mathbf{E} \cdot \mathbf{B}$ takes a nonzero value. Even before the concept of reconnection was introduced, it had been conceived that the flux-conservation condition may break down in the presence of a finite $\mathbf{E} \cdot \mathbf{B}$ (Newcomb 1958). Non-zero $\mathbf{E} \cdot \mathbf{B}$ is now regarded as a necessary condition for reconnection regardless of the presence of a null-point (Schindler et al. 1988; Hesse and Schindler 1988). $\mathbf{E} \cdot \mathbf{B}$ is also the source term in the helicity evolution equation (Berger 1984; Berger and Field 1984) and we suggest that the rotational flows in 3D reconnection are a signature of the helicity production or decay. An exception occurs for 2D reconnection, however, because a magnetic field and its motion lying on a 2D plane makes an electric field out of the plane, and no magnetic component can be specified in that direction. The zero $\mathbf{E} \cdot \mathbf{B}$ in this case does not mean no reconnection possible in 2D, since both $\mathbf{E} \cdot \mathbf{B}$ and $|\mathbf{B}|$ are zero at an X-point, and $E_{\parallel} = \mathbf{E} \cdot \mathbf{B}/|\mathbf{B}|$ can be finite. Therefore, the nonzeroness of $\mathbf{E} \cdot \mathbf{B}$ does not apply to 2D reconnection and can be a criterion for the dimensionality of magnetic reconnection.

Let us apply this condition to the two specific magnetic configurations for solar flares. In a magnetic arcade system (Fig. 2c) consisting of 2D X-configuration lying on the x–z plane stacked along the PIL in the y-axis, magnetic field is expressed as $(B_x, 0, B_z)$. In that system, field line motion on the x-z plane produces an electric field in the y-axis, E_y, and $\mathbf{E} \cdot \mathbf{B}$ is zero so that reconnection proceeds in a 2D manner. If a nonzero guide field, B_y, is added, the system will change to a sheared arcade and 3D reconnection is enabled. Note, however, that in the sun an unshared arcade evolves to a sheared arcade via footpoint motion under the line-tying condition. This process may not necessarily be the same as turning on a guide field in numerical or laboratory experiments in that the whole arcade system can be sheared or distorted in a way to form another set of 2D systems. Until the 3D components of field line motion around the X-point is known, we cannot guarantee 3D reconnection solely based on a 3D magnetic structure.

Likewise, the circular fan-dome configuration (Fig. 2d) has magnetic field components only in the r-z plane, (B_r, 0, B_z), so that a field line motion in the plane will create E_θ. Again, 3D reconnection is not really possible in this case, albeit its perfect 3D appearance. Only when the fan field is torsionally distorted to create the B_θ component, $\mathbf{E} \cdot \mathbf{B}$ is nonzero and 3D reconnection will occur. To call such B_θ a torsional component, and such B_y a shear component, we notice that both torsional and shear components are in the direction of the PILs of the respective systems. We can therefore expect that solar flares occuring in the presence of magnetic field parallel to PIL are likely to be involved with 3D reconnection and, otherwise, with 2D reconnection. Alternatively we may test the nonzeroness of $\mathbf{E} \cdot \mathbf{B}$ based on flare ribbon motions, which may allow a more practical approach in solar physics.

3.2 Reconnection rate and energy conversion rate

In the general framework of 3D magnetic reconnection (Schindler et al. 1988; Hesse and Schindler 1988), the change of connectivity, or the flux reconnection rate, is quantified by the maximal value of

$$\dot{\Phi}_{\rm rec} = \int \frac{\mathbf{E} \cdot \mathbf{B}}{|\mathbf{B}|} \, {\rm d}l = \int E_\parallel \, {\rm d}l, \tag{2}$$

where the integration is performed along any field line threading the non-ideal region from one side of the diffusion region to the other. In the 2D standard model, $E_\parallel$ can be determined by the ribbon speed and normal magnetic field strength, and the product of those two quantities is typically referred to as the magnetic reconnection rate in solar flare studies (Fig. 1g). For 3D reconnection rate no simple analytical expression is yet available, and we will discuss this issue in this section.

For astrophysical applications, the amount of energy released by reconnection may be more important than the rate of reconnecting flux. For the interest of physicists, another quantity called dimensionless reconnection rate is more important, because it tells the efficiency of reconnection. A goal is this section is to express the energy conversion rate in terms of solar observables and the dimensionless reconnection parameters. Commonly used for the calculation of the energy conversion rate is the Poynting flux (Isobe et al. 2005). Since the Poynting vector represents the power flow of an electromagnetic field or the directional energy transfer per unit area per unit time, total electromagnetic energy change rate $\dot{\mathcal{E}}_B$ can be expressed as follows if it is solely due to the Poynting vector, $\mathbf{S} = \mathbf{E} \times \mathbf{B}$, coming from both sides into the nonideal region with area $\mathbf{A}$:

$$-\dot{\mathcal{E}}_B = 2 \int \mathbf{S} \cdot {\rm d}\mathbf{A}. \tag{3}$$

The issue is therefore how to specify an appropriate area $\mathbf{A}$ through which $\mathbf{S}$ flows out of the diffusion region.

To derive the simplest possible expressions for these two key parameters, we use the schematic geometry plotted in Figs. 4 and 5. The figures show the field lines

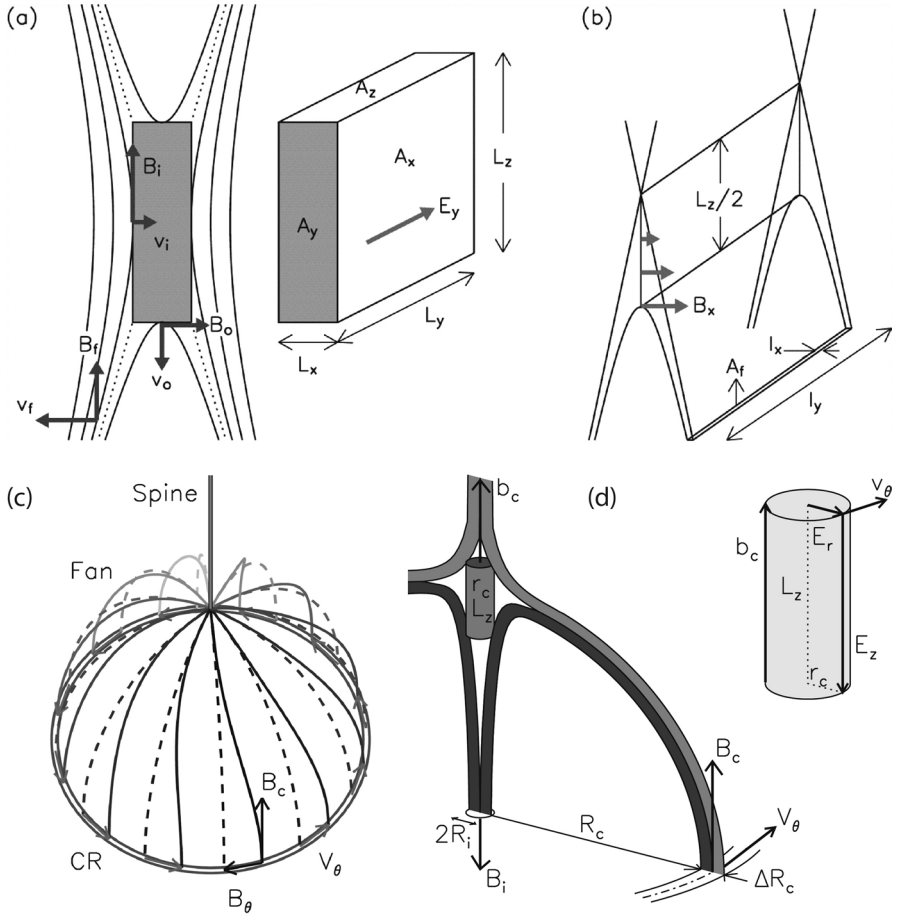

Fig. 4 Parameters used for formulating magnetic reconnection in PRF (**a**, **b**) and CRF (**c**, **d**). **a** An arcade system for 2D X-point inside the current layer (shaded area) and the separatrix (dotted lines). **b** The relationship between the coronal current layer and the flare ribbons. (Source: Lee et al. 2006). **c** A spine-fan system with (solid) and without (dashed) a torsional perturbation. **d** Layers of the fan fields connecting from the CR to the outer spine (light shade) and to the inner spine (dark shade) along with the current tube located around the 3D null point

in ideal regions (solid lines) and nonideal regions (gray shaded volumes) along with the motions associated with each type of reconnection for two types of magnetic configurations: a magnetic arcade (Figs. 4a, b, 5a, b) and a spine-fan system (Figs. 4c, d, 5c–f). The formulation to be presented in this section is based on the relationship between these geometrical parameters to those of ribbon structures observable in solar surface.

3.2.1 X-point reconnection

Figure 4a, b shows the magnetic field configuration for formulating 2D reconnection. The X-point is actually hidden inside the diffusion (or nonideal) region colored gray. For our purposes, we need a finite volume of the nonideal region as will be discussed below. Let us use subscripts, i, for parameters associated with the incoming field into the X-point, o for the outgoing field, and f for the footpoint field, i.e., ribbons. In the coordinate system shown in Fig. 4a, the 2D reconnection occurs at the X-point and the associated electric field is $E_y = -v_x^i b_z^i$ in the direction out of the x-z plane. This leads to

$$\dot{\Phi}_{\rm rec} = \int_0^{L_y} E_y \mathrm{d}L_y = \int_0^{L_y} v_f B_f \mathrm{d}L_y \approx v_f B_f l_y, \tag{4}$$

where $v_i B_i$ is replaced by $v_f B_f$ under the principle of magnetic flux conservation. Another note is that the X-line length, L_y, in the corona is set to be the same as the ribbon length, l_y in the photosphere. Both $v_i B_i = v_f B_f$ and $L_y = l_y$ are the key elements of the 2D reconnection, which allow us to calculate the coronal reconnection rate with solar observables only (Forbes and Priest 1984; Priest and Forbes 2000; Forbes and Lin 2000). We may accommodate an inhomogeneous ribbon structure by allowing E_y to vary along y-direction and allow the integral path to be arbitrarily curved. Namely, we can stack the 2D slices along the y-axis to make it 2.5D while keeping the X-point reconnection physics valid. This form of reconnection rate has been the most widely used in solar flare studies.

The 2D magnetic field configuration and other physical parameters around the reconnecting current sheet (RCS) are shown in the left panel (Fig. 4a). The separatrices are shown as dotted lines and the RCS, as the shaded slab centered at the X-point. The Poynting flux coming from one side is $\mathbf{S}_i = \mathbf{E}_i \times \mathbf{B}_i = E_y B_i \hat{x}$. The total electromagnetic energy change solely due to the Poynting fluxes coming from both sides into the RCS is then expressed by:

$$-\dot{\mathcal{E}}_{\rm rec} = 2E_y B_i A_x = 2v_i B_i^2 A_x. \tag{5}$$

To complete the calculation we need $A_x = L_y L_z$, the current sheet area. In 2D configuration, L_y is equivalent to the ribbon length, but L_z is not directly observable. Lee et al. (2006) linked L_z to L_x via the dimensionless reconnection rate, M, defined by the ratio between the inflow to outflow speed (Petschek 1964). According to their RCS geometry and some simplifying assumptions, this ratio is, in fact, simply the aspect ratio of the RCS:

$$M \equiv \frac{v_i}{V_A} = \frac{L_x}{L_z} = \left|\frac{B_o}{B_i}\right| < 1. \tag{6}$$

They applied the flux conservation law not only to the incoming B_z component but to the outgoing B_x component in the RCS. Namely, the magnetic flux through the ribbon area, A_f, equals the flux going through A_x as:

$$B_x L_y \frac{L_z}{2} = B_f A_f. \tag{7}$$

The factor of 2 arises because B_x is assumed to vary linearly from $B_x = B_o$ at the bottom of the RCS to $B_x = 0$ at the X-point Fig. 4b. We also have $A_x B_o = 4 B_f A_f$ from the flux conservation law. What we need to know to close this calculation is therefore a relationship between B_o and B_i. Lee et al. (2006) used Eq. (6) to remove B_o to express the magnetic energy release rate in terms of solar observables:

$$\dot{\mathcal{E}}_{\rm rec} = -\frac{8 B_f^2 A_f}{M} |v_f|. \tag{8}$$

One simplifying assumption for this expression is that most of the incoming energy flux ($S_x A_x$) should be consumed inside the RCS and the outgoing energy flux ($S_z A_z$) carry a negligible amount of energy as is likely for solar flares (see, for justification, Lee et al. 2006). Goodbred et al. (2021) presented a more thorough calculation of the energy conversion rate without such approximation. Our intention for this simple expression is that the observed ribbon area can be used instead of the unknown RCS area along with the dimensionless reconnection rate, M.

3.2.2 Torsional reconnection

Torsional reconnection, although has been in the focus of 3D reconnection studies, has not yet attained analytical expressions for the reconnection rate. A major difficulty in formulating torsional reconnection rate is that the flux-transporting flow into the nonideal region is actually decoupled from the counter-rotational flow that determines the reconnection rate (Hornig and Priest 2003). We thus proceed with the premise that a theoretical assessment of the reconnection rate and energy conversion rate is not possible as far as torsional reconnection is concerned.

As shown in Fig. 4c, we consider that a torque is applied on the CR to perturb the fan field lines in the θ direction. As a result, a current region develops along the spine around the null. In this so-called torsional spine reconnection, the reconnection rate should be

$$\dot{\Phi}_{\rm rec} = \int E_\parallel^* {\rm d}s \approx 2 L_z E_z, \tag{9}$$

where $E_\parallel^*$ is the reconnection electric field parallel to the spine. The nonideal region is assumed to be in the form of a cylindrical tube with height L_z and radius r_c (Fig. 4d). A loop integral of the electric field around the tube under Faraday's law will allow us to replace $L_z E_z$ with $-r_c E_r$. We can then rewrite the above quantity as $\dot{\Phi}_{\rm rec} = -2 r_c b_c v_\theta^*$. Here v_θ^* is the counter-rotational flow motion during reconnection, which is unknown to us. Instead we can specify v_θ for the rotational flow motion driven externally. The above issue can be rephrased as $v_\theta^* \neq v_\theta$, which means that information on torsional reconnection is inaccessible.

Contrary to the general belief, we can, at least, specify the flux input rate supplied by the driver, $\dot{\Phi}_{{\rm d}rv}$ by using v_θ instead of v_θ^*. Upon time integration of $\dot{\Phi}_{{\rm d}rv}$, we

can determine the total amount of flux available for torsional reconnection, which must be comparable to the reconnected flux, i.e., $\dot{\Phi}_{drv}\tau_{drv} = -\dot{\Phi}_{rec}\tau_{rec}$ where τ_{drv} is the timescale for driving the magnetic twist and τ_{rec}, for reconnection. To determine $\dot{\Phi}_{rec}$ from this relation, the only missing piece of information is τ_{rec} representing timescale for the counter-rotational flow motion. To cope with this issue, we introduce an ad hoc parameter:

$$\alpha \equiv \frac{\tau_{drv}}{\tau_{rec}} = \frac{v_\theta^*}{v_\theta}. \tag{10}$$

With this yet-unspecified parameter, we will explore properties of torsional reconnection to the extent that they are controlled by an external driver. For now, our goal is to calculate the flux reconnection rate in the form:

$$\dot{\Phi}_{rec} = \alpha \int E_\parallel \mathrm{d}s = -2\alpha r_c v_\theta b_c. \tag{11}$$

In Fig. 4d, we set a circular fan with radius R_c and footpoint field strength B_c. The spiral shape of the fan field shown in Fig. 4c is omitted in Fig. 4d for visual simplicity, as is not essential for applying the flux conservation relation. In this case, the flux conservation law gives:

$$r_c^2 b_c = 2R_c B_c \frac{\triangle R_c}{2}, \tag{12}$$

where the factor of 2 appears in the denominator because we split the CR into two parts: one connected to the outer spine (light shaded layer) and the other to inner spine (dark shaded layer). We assume a rigid (even though not) rotation to have $v_\theta = r_c(V_\theta/R_c) = r_c\dot{\theta}_c$. This relation along with the flux conservation law allows us to express the torsional reconnection rate:

$$\dot{\Phi}_{rec} = \alpha \frac{\dot{\theta}_c}{\pi} B_c A_c. \tag{13}$$

in terms of α representing the yet unknown physics of field line slippage along with other parameters specifying the torsional driver.

For calculation of energy, we utilize two kinds of Poynting vectors available in the present setting. The first Poynting vector is created by a torque applied to CR. Due to the rotation of footpoints at V_θ, a radial component of electric field, $E_r = -V_\theta B_c$, and then upward Poynting vector, $S_z = -E_r B_\theta = -V_\theta B_\theta^2$, are created. This Poynting vector is distributed over the CR area, $A_c = 2\pi R_c \triangle R$, and propagates toward the null along the fan field (Fig. 4d). Since a fan field line forms a half circle in the (r, z) plane, the Poynting vector is S_z at the start and becomes S_r reaching the null point. This process can be more easily visualized by using the flattened fan surface onto the (r, θ) plane (Fig. 5d). Therefore, the enhanced magnetic energy in the fan region transported to the nonideal region per unit time is

$$\dot{\mathcal{E}}_{\mathrm{d}rv} = -\int \hat{r}\cdot\mathbf{S}\,\mathrm{d}A = -\int S_z\,\mathrm{d}A_c = B_\theta^2 A_c V_\theta = \frac{\mathrm{d}}{\mathrm{d}t}B_\theta^2\mathcal{V}_c \tag{14}$$

where $\mathcal{V}_c = (\pi R_c^2)\bigtriangleup R_c$ is the volume of the circular disk shown in Fig. 5d. This is rather an obvious result, since the system will lose the extra energy gained by an external torque via derotation of the fields to restore the original state. What matters is, of course, the timescale. It also clarifies that without B_θ, there is no energy flux toward the nonideal region and no torsional reconnection (see also Sect. 3.1.3).

The second Poynting vector is calculated using the counter-rotational motion, v_θ^*, as defined above. The electric field $E_r = v_\theta^* b_c$ and the magnetic field b_c in the nonideal region gives a rotating Poynting vector, $S_\theta = v_\theta^* b_c^2$, which passes through the cross sectional area, $L_z r_c$. The associated energy change rate is $\dot{\mathcal{E}}_{\mathrm{rec}} = -\alpha v_\theta b_c^2 r_c L_z$, which we can relate to observables by utilizing the flux conservation law [Eq. (12)], but not L_z. We thus introduce another dimensionless parameter:

$$N \equiv \frac{r_c}{L_z}, \tag{15}$$

in an analogy to $M \equiv L_x/L_z$ in 2D. The energy flow rotating inside the nonideal region about the spine is then $\dot{\mathcal{E}}_{\mathrm{rec}} \approx -B_c^2 A_c \bigtriangleup R_c |V_\theta|/\pi N r_c$. It is likely that the diameter of the nonideal tube is comparable to the width of CR if the field strength of CR is comparable to that of IR, $B_c \sim B_i$. We thus make an approximation, $2r_c/\bigtriangleup R_c \approx 1$, to further simplify the expression to the following form:

$$\dot{\mathcal{E}}_{\mathrm{rec}} = -\alpha\frac{B_c^2 A_c}{\pi N}V_\theta. \tag{16}$$

As a note, one may ask whether or not this quantity without α must match the energy input rate in Eq. (14), because the Poynting energy in the ideal region should be conserved before reconnection. Since the driving Poynting flux, S_r, is coming toward the spine in all directions, it has to turn into S_θ reaching the spine making itself vulnerable to torsional reconnection. Therefore, the magnitude of $S_r A_r$ originating from the CR should be the same as that of $S_\theta A_\theta$ rotating about the spine. By equating (14) with (16), we find $N \sim \alpha\theta^{-2}$. Namely, a stronger driver ($\sim \theta^2$) makes the tube more slender, and at a faster torsional reconnection rate ($\sim \alpha$), it becomes less slender.

At this point, we can proceed no further, until how the magnetic twist energy escapes out of the nonideal region is known. In our configuration (Fig. 4d), S_θ does not cross any surfaces of the nonideal tube. S_θ must turn itself into S_z as part of the torsional reconnection process. This flipping in the orientation is not in the present formulation, but is likely to occur in view of the MHD simulations indicating torsional Alfvén waves (e.g., Wyper and Jain 2011; Wyper et al. 2017) or helical jets (Pariat et al. 2015) propagating out of a CRF region (Fig. 5c).

We summarize the energy transfer around torsional reconnection based on the Poynting theorem:

$$\frac{\partial u}{\partial t} = -\nabla\cdot\mathbf{S} - \mathbf{J}\cdot\mathbf{E}, \tag{17}$$

where u is energy density and $\mathbf{J}$ is current density in the system. Equation (14) represents the input energy due to S_r, delivered to the nonideal region without any loss. As S_r is coming from all radial directions, it gets involved rotational motion reaching the spine to produce S_θ, which amounts to an angular momentum trapped inside the nonideal region [Eq. (16)]. During the torsional reconnection, S_θ is likely to be turned into S_z, so that it can escape out along the spine at the rate of $\partial S_z/\partial z$, and part of the energy will be dissipated via Joule heating, $\mathbf{J}\cdot\mathbf{E}$. This energy conversion process, as is determined by the torsional reconnection, remains undetermined. We could, at least, present the maximum energy input rate to the nonideal tube, $\partial u/\partial t$, available for release under the torsional reconnection.

3.2.3 Spine-fan reconnection

Spine-fan reconnection may be a more common type of reconnection in a spine-fan structure, and presents a couple of other difficulties in relating the field line slippage to the energy conversion rate. First of all, a spine will interact with a section of fan, which will apparently result in an asymmetric distribution of the magnetic flux in an otherwise symmetric spine-fan structure. During such reconnection, a CR can expand on one side and contract on the other side, a phenomenon schematically illustrated in Fig. 5e, f. Another difficulty is that the field line slippage speed near a spine can be arbitrarily large, because mapping of field lines near the spine to their footpoints can be discontinuous. Both properties are well demonstrated by a 3D MHD simulation by Pontin et al. (2013), and make it challenging to formulate the reconnection rate and energy conversion rate. However, the inward and outward shift of CR from its original position during spine-fan structure should somehow be related to the magnetic flux transfer into and out of the dome structure (Masson et al. 2017), unlike the torsional reconnection for which such a relationship could not be set.

To accommodate the asymmetric connectivity change in the r-z plane, we separate the ribbon motions in two domains: in D^+, the CR is moving outward from the original position, and in D^-, the ribbon is coming inward from the original position. In D^+, we use the notation, $\triangle R^+$, for the local ribbon width and $V_R^+ = \mathrm{d}\triangle R^+/\mathrm{d}t$ for the radial expansion rate of CR. We reuse the same flux conservation law [Eq. (12)] but with an additional sign for distinguishing between the two domains, i.e., $b_c r_c^2 = B_c R_c \triangle R^\pm$. By differentiating this equation with respect to time, we obtain the electric field as $E_\parallel^+ = b_c \dot{r}_c = B_c R_c V_R^+/r_c$ in D^+ and $E_\parallel^- = -B_c R_c V_R^-/r_c$ in D^-, where we put the minus sign to denote the contraction of the CR and keep $V_R^\pm$ as positive numbers. The two electric fields in $D^\pm$ are thus oppositely directed:

$$E_\theta^\pm = \pm\frac{B_c|V_R^\pm|R_c}{r_c}. \tag{18}$$

Note that $E_\theta^\pm$ diverges at $r_c = 0$, i.e., near the spines, but upon the integration of $E_\theta^\pm$ over $dl = r_c d\theta$, we find the flux reconnection rates as finite as

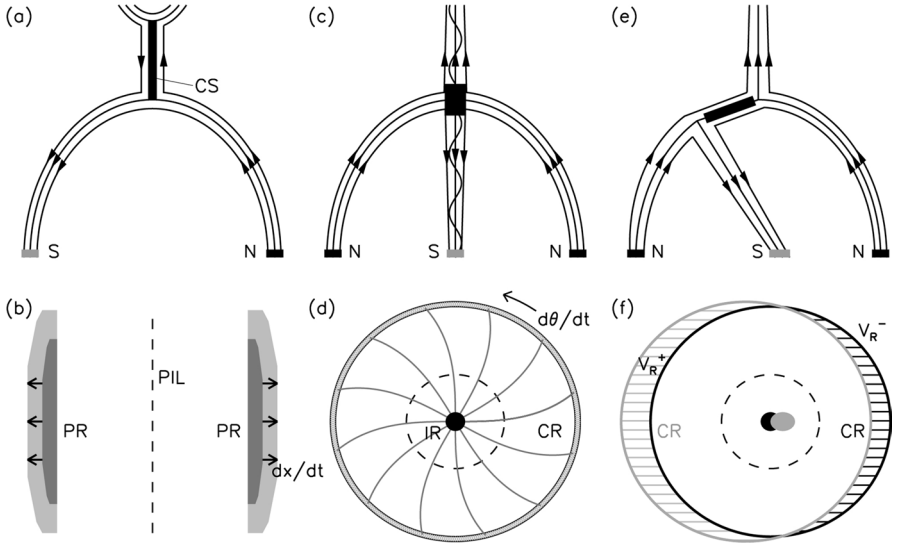

Fig. 5 Schematic illustration of the three types of reconnection: 2D X-point (**a**, **b**), torsional (**c**, **d**), and spine-fan (**e**, **f**) reconnection. Upper panels show the side views of the magnetic configurations in which N and S refer to the magnetic polarity in the footpoints and the filled arrows, the polarity of the coronal fields. The black regions in the corona represent the nonideal region. Lower panels show the top-down views in which three types of ribbons, PR, CR, and IR are denoted together with their motions in the translational, rotational, and vibrational degrees of freedom. Dashed lines are PILs

$$\dot{\Phi}^{\pm}_{\rm rec} = \int_{D\pm} E^{\pm}_{\theta} dl^{\pm} = 2\pi R_c V^{\pm}_R B_c = \dot{A}^{\pm}_c B_c, \tag{19}$$

which is apparently similar to that of the 2D reconnection rate with a different notation of $V^{\pm}_R$ for the inward and outward ribbon motions. The reason why we end up with the same sign for $\dot{\Phi}^{\pm}_{\rm rec}$ is that the two domains, $D^{\pm}$, are connected to the upper and lower spines, respectively, and the integral path in D^- has the opposite sense to in D^+, i.e., $\mathrm{d}l^- = -\mathrm{d}l^+$. Both are the flux change rates in the same magnetic polarity. The sum of them should match the flux change rate of their pairs in the other magnetic polarity, i.e., IR and a remote ribbon. Here the difference between $\dot{\Phi}^{\pm}_{\rm rec}$, is just complementary to each other as they represent a flux transfer from one domain to the other.

We come back to the issue of diverging E_θ at small r_c as noted in Eq. (18), which must be related to the discontinuous field line mapping near the spine. The path integration can be performed up to a very small distance from the spine, but not at the spine itself, at which point we are unable to specify the rate of field line slippage in terms of its footpoint motion. This slippage rate becomes arbitrarily high because two neighboring field lines near the spine can possibly be connected to widely separated footpoints. We argue that this issue arises when we trace individual field lines one by one. If we trace a group of field lines as an integral quantity, we can still relate the reconnecting area to the ribbon area. In this sense, the above

quantity [Eq. (19)] obtained under 2D decomposition can serve as an average of the 3D reconnection rate along r_c.

In this setup, the Poynting flux inwardly propagating into the nonideal region is given by $E_\theta b_c$ (Fig. 4d). In the above, we have already worked out $b_c = B_c R_c \bigtriangleup R/r_c^2$ [Eq. (12)] and $E_\theta^\pm = \pm B_c V_R^\pm R_c/r_c$ [Eq. (18)]. The area of the nonideal region where the Poynting flux passes through is $2\pi r_c L_z$. To replace r_c with solar observables, we define another parameter, K, as

$$K \equiv \frac{r_c}{R_c} \approx \frac{R_i}{R_c}. \tag{20}$$

The latter approximation assumes that the nonideal tube is straightforwardly projected onto IR so that r_c is close to the IR radius. In this case, K is practically given by the ratio of the CR radius (R_c) to the IR radius (R_i), which represents the overall structure of a CRF. We finally express the energy conversion rate for the spine-fan reconnection as

$$\dot{\mathcal{E}}_{\rm rec} = -\frac{B_c^2 A_c V_R^\pm}{NK}, \tag{21}$$

where $A_c = 2\pi R_c \bigtriangleup R$ is the area of CR. $V_R^\pm$ can be regarded as the change rate of the area, A_c, and the areal change in this case comes from that of the CR width, $\bigtriangleup R$, since we set $R = \langle R\rangle + \bigtriangleup R$ with time-invariant $\langle R\rangle$ representing the original position of the CR. Aside from N, we are able to describe the spine-fan reconnection in terms of the inflow and outflows, $V_R^\pm$, around the fan and a geometrical factor, K, of IR to CR, as expected.

To clarify which assumptions lead to such simple expressions for the spine-fan reconnection [Eqs. (19, 21)], we first note that we separately treated the ribbon motions in the two domains, $D^\pm$, but did not explicitly introduce the asymmetric location of the current sheet into the formulation. In reality, a current sheet resides on one side of the fan causing expansion of CR on that side and contraction on the other (see, for 3D simulation results, Fig. 9). Another important element missing in our formulation is the geometry of the current sheet lying between the interacting spine and fan (Fig. 5e). We simply treated it as a small ring around the null. As a result, this energy conversion rate [Eq. (21)] does not contain a dimensionless parameter representing the current sheet geometry, unlike that of 2D X-point reconnection [Eq. (8)] and torsional reconnection [Eq. (16)]. A more rigorous formulation is underway, but in the present paper, we limit the scope of investigation to the average effect of the spine-fan reconnection on the positional shift of CR.

3.3 Degrees of freedom

We put together the above results in Table 1 where (1) degrees of freedom, (2) dimensionless parameters, (3) reconnection rates, and (4) energy conversion rates are specified for the three types of reconnection: X-point, torsional and spine-fan

Table 1 Rates of magnetic reconnection and energy conversion

	X-point	Torsion	Spine-fan
Degree of freedom	Translation	Rotation	Vibration
Dimensionless parameter	$M \equiv v_i/V_A$ [a]	$\alpha \equiv \tau_{drv}/\tau_{rec}$, $N \equiv r_c/L_z$	$K \equiv r_c/R_c$
Flux reconnection rate	$V_f B_f L_f$ [b]	$\alpha\dot{\theta} B_c A_c/\pi$	$2\dot{R}_c B_c A_c/R_c$
Relative flux change rate	$\dot{D}/D$	$\alpha\dot{\theta}/\pi$ [d]	$\dot{R}^2/R^2$
Energy conversion rate	$8B_f^2 A_f v_f/M$ [c]	$\alpha B_c^2 A_c V_\theta/\pi N$	$B_c^2 A_c V_R^{\pm}/\pi NK$

[a]Petschek (1964)

[b]Forbes and Priest (1984)

[c]Lee et al. (2006)

[d]Physics of α is unknown

reconnection. These quantities derived for the steady state clarify which motion is involved with each type of reconnection, and how they are related to solar observables. We here discuss these results to provide insights into the dimensionality of solar magnetic reconnection.

Table 1 also provides a simplified categorization of the existing ideas on solar reconnection according to the degree of freedom. It is worthwhile to clarify once again why no attempt had been made to derive such analytic expressions, except those for the X-point reconnection in 2D. The main reason is that tracing individual field lines in 3D reconnection is not as straightforward as in 2D (Sect. 3.1). We have instead exploited the one-to-one relationship that still holds for the two major quantities, the flux reconnection rates and energy conversion rates, integrated over the whole ribbon area. In that spirit, the expressions listed in Table 1 are more suitable for facilitating qualitative discussions of solar 2D and 3D reconnection. Note also that no theory for α is yet available, and the quantities for torsional reconnection with $\alpha = 1$ correspond to the input rates of flux or energy available for reconnection rather than the output rates of reconnection.

Unfortunately the flux reconnection rate strictly depends on the system size and field strength, and it is less meaningful to compare these quantities in two systems with different size and field. As a way of normalization, we divide them by the corresponding magnetic flux. We call them relative flux change rates and list them in the next row. These quantities simply mean that the reconnection efficiency is controlled by the translational speed and the rotational speed, respectively. Similarly, we may want to normalize the energy conversion rates by the corresponding energy. It is more cumbersome because the field strength in the nonideal regions instead of the ribbon field should be specified. It is, however, obvious that such normalized energy conversion rates would be in the form of the change rate of the nonideal region volume.

As an aid to interpretation of these analytical expressions, we present, in Fig. 5, schematic illustration for the three types of reconnection in the side view (upper row) and top-down view (bottom row). The 2D X-point reconnection (Fig. 5a, b) is plotted mainly to indicate that it involves translational motion. The black regions represent the current sheet where reconnection occurs. The upward motion of the

X-point is related to the ribbon separation motion, and the expansion of the current sheet is related to the ribbon expansion, both of which are key observables in the solar standard 2D flare model. Figure 5c shows a circular dome-shaped fan and two spines. Torsional reconnection occurs within the current layer in the form of a tube (black region) located around the 3D null. We plot the wavy structure for representing torsional Alfvén waves or helical jets. Figure 5d shows a top-down view of the circular dome-shaped fan to emphasize that a non-zero B_θ created by an external torque, $\dot{\theta}$, is essential to bring up the rotational degree of freedom.

Figure 5e shows a configuration for spine-fan reconnection. The outer spine is interacting with a section of the fan flux across the current sheet (black region), which results in an asymmetric flux distribution. In Fig. 5f, the black circle represents the location of the original CR, and the gray circle, that of CR after the reconnection. Depending on which side the spine and fan are in contact, CR expands on that side at the speed V_R^+ and shrinks on the other side at V_R^-. IR plotted in the same color convention also exhibits a shift in position. Such an asymmetric sectional variation is abbreviated to an areal variation, $\dot{R}^2$, in our simplified expression. We compare this motion to a vibrational degree of freedom.

3.4 Dimensionless parameters for reconnection

The three dimensionless parameters, M, N, and K, introduced in this study are technically needed in order to set the geometry of the nonideal region, when we relate the nonideal region to the ribbon area through the Poynting flux. Interestingly, they are not needed for the flux reconnection rates, because fluxes in both regions are directly related to each other under the flux conservation law. We wish to point out that these dimensionless parameters also carry implication on the degrees of freedom associated with the types of reconnection.

M is the key parameter in the 2D reconnection theory, as it represents the efficiency of reconnection regardless of the system size and magnitude of the magnetic field. Physicists are interested in universal laws that apply to all scales, say, from an explosive event in a galaxy to that of a matchbox. M is defined by the ratio of inflow to outflow speed or, equivalently, the aspect ratio of the nonideal region, which tells how many field lines coming in and out of it. Expectedly $M \approx 0.1$, and finding this value is a long-term wish in solar observations and laboratory experiments (Yamada et al. 2004; Yan et al. 1992; Yokoyama et al. 2001).

N also represents the geometry of a nonideal region undergoing torsional reconnection like M does for X-point reconnection. Upto this point, we mainly discussed torsional spine reconnection for which $N < 1$ and N decreases further at a stronger torque applied on the fan. For torsional fan reconnection $N > 1$, and perhaps N increases at a stronger torque applied on the spine. The mostly unknown parameter is α, which couples the flux-transporting flow into the nonideal region to the counter-rotational flow that determines the reconnection rate. It is certainly desirable to attempt an empirical determination of α either by solar observations or by numerical and empirical experiments. There is, however, no guarantee that α should be a

constant or a smooth function of observable quantities. α might even behave like a step-function in case that the field line untwisting occurs in a manner of instability.

K is somewhat different from M and N in that it represents the overall structure of a CRF. It is yet unknown whether IR radius tends to be proportional to CR radius or is solely determined by some fundamental physics. Since the fan surface in a CRF is rooted in the surface to act like a drum, K may be understood as analogous to the size ratio of a drum stick to the drum, which would certainly matter in the drum vibration. In this case too, the aspect ratio of the current sheet forming between a spine and a fan should have been introduced to better quantify the spine-fan reconnection. This is graphically illustrated in Fig. 5c, but greatly simplified in our formulation. An elaboration of this formulation is in progress.

A remaining issue is, of course, how to determine these dimensionless parameters. In most astrophysical studies, the amount of magnetic energy released via reconnection is of utmost importance, and one may want to use M predetermined from independent theory or laboratory experiments in calculation of the energy. One may, alternatively, want to determine the dimensionless parameters, if the physics of reconnection efficiency is of the primary interest. We once thought that M could alternatively be determined by equating the energy conversion rates to independently measured energy conversion rates from hard X-ray spectra (Lee et al. 2006), which is still underway. Similarly, one may attempt an empirical determination of α with solar observation by measuring both the rotational flows entering the nonideal tube and those coming out of the tube so that we can relate their difference to the torsional reconnection rate. It must be a highly challenging task, but the energy released by the untwisting field lines is likely to be observable in the form of torsional Alfvén waves (e.g., Wyper and Jain 2011; Wyper et al. 2017) or helical jets (Pariat et al. 2015) that escape out of CRF regions.

4 Magnetic reconnection in spine-fan structure

Much of the initial interest in 3D magnetic reconnection was due to the desire to understand how the reconnection occurs in a single null point topology. For this topic, solar research has largely relied on a number of numerical simulations (Rickard and Titov 1996; Galsgaard and Nordlund 1997; Galsgaard et al. 2003; Pontin and Galsgaard 2007; Pariat et al. 2009, 2010; Masson et al. 2009, 2017; Pontin et al. 2007), in a fan-spine structure that hosts CRFs. As a result, the following processes in CRFs are currently identified: (1) When the fan/spines are distorted as a result of shearing or rotational perturbations, current sheets develop at the null point or along the fan (Pontin and Galsgaard 2007). (2) When stress from rotational motions is constantly applied, recurrent reconnection at the null point may occur (Pariat et al. 2010). (3) Shearing the spine is effective in generating intense electric currents at the null point (Masson et al. 2009) and the induced reconnection has an effect to restore the alignment of the spines (Antiochos et al. 2002). (4) Magnetic reconnection in the current sheets formed

at the null can be triggered by either small-scale local instabilities, e.g., tearing instabilities (Masson et al. 2009; Archontis et al. 2005; Shibata and Tanuma 2001) or large-scale instabilities, e.g., kink-like instability (Pariat et al. 2009, 2010, 2015).

In this section, we mainly discuss magnetic reconnection in a CRF-producing spine-fan structure. This is, of course, not the only structure that can possibly host 3D reconnection, and the spine-fan reconnection is not the only possible mode of reconnection in a spine-fan structure. We assert that a variety of modes including the torsional and a hydrid reconnection may occur in a solar fan-spine system. To organize those various reconnection modes we utilize the generic 3D kinematic models developed by Priest and Titov (1996), Pontin et al. (2004, 2005a, b), Pontin (2011, 2012), and Pontin and Priest (2022). The reader should keep in mind that solar flares occurring in more complex configurations than those prescribed by the theoretical models, may have a mix of multiple modes of reconnection.

4.1 Null current parallel to spine

Torsional reconnection due to null current with a particular orientation is a theoretical invention with somewhat arbitrary choices of the driver. It can be debatable whether the sun can actually provide a suitable driver. It is rather unlikely that a large driver appears on the sun to coherently rotate the fan to let the null current build up parallel to the spine. Nonetheless we here present a flare event, which is characterized by a large fan structure surrounded by a coronal hole, in which case any perturbations such as emergence of a sunspot or its rotation may push the fan field against the coronal hole boundary to provide an effective twist needed for torsional reconnection.

We reproduce the theoretical kinematic model of Pontin (2011, 2012) in the left panels, and the flare event in the right panels of Fig. 6. The kinematic model (Fig. 6a–d) shows that the counter-rotational flows are centered on the spine and the change of connectivity resulting from the reconnection process therefore takes the form of a rotational slippage (Pontin et al. 2004; Wyper and Jain 2011). For comparison with solar flares, we should bend such a fan surface down toward the surface to form the CR (Fig. 1), and compare the rotation of the red/blue tubes in the left panels with the brightness propagating along a CR in the right panels.

Shown in Fig. 6e is one such event of slipping motion along CRs (Lim et al. 2017). The large CR indeed exhibits a slippage motion predicted by the theoretical kinematic model. Although the moving brightness along CRs is visually obvious but not necessarily suitable for quantitatively measure. The event shown here is a particularly large CR centered in NOAA AR 12371 and partially bounded by a large coronal hole (surrounding darker emission), which makes the rotation slippage prominent. Authors themselves called this CR the secondary circular ribbon because it is so large. They regard the ribbons in the center of the active region as primary. Such a complexity is not uncommon in the sun. Even a double CRF, namely, a CRF

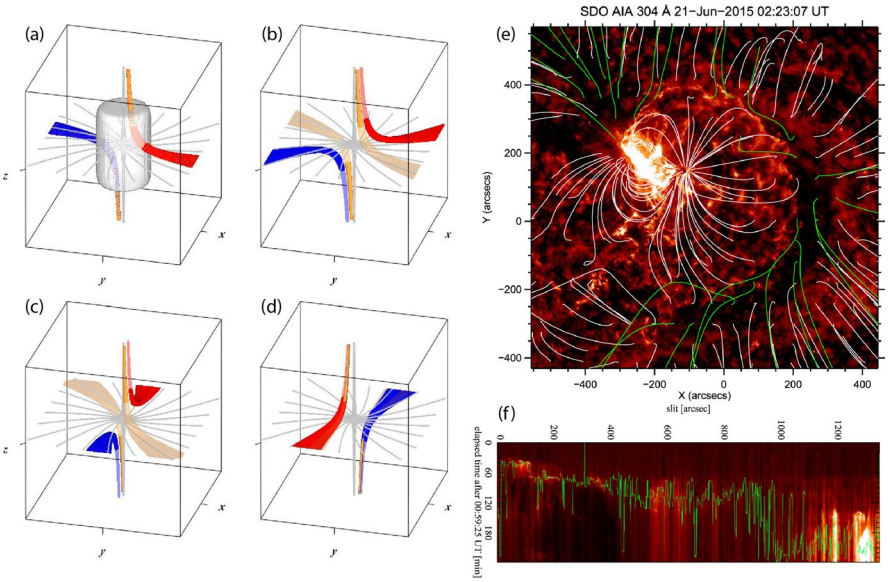

Fig. 6 Torsional spine reconnection. In the theoretical model (**a**–**d**), flux tubes traced from four ideal comoving footpoints come into a localized diffusion region (gray surface) around the null point and rotate in the plane perpendicular to the spine (Source: Pontin 2011). In an observational example, the 2015-06-21 flare from NOAA AR 1237 (**e**, **f**), such a rotational motion in the fan appears as a slippage motion along a CR. The closed field lines (white) and open field lines (green) obtained from the PFSS model are overplotted on AIA 304 Å image (**e**). The local intensity maxima (green line) in the time-distance map (**f**) is used to estimate the ribbon speed, 161 km s^{-1}. Source: Lim et al. (2017)

emerges within another larger CR has been reported (Li et al. 2018a; Hou et al. 2019). A nested structure of either CR or PR often appears in the sun.

Figure 6e also shows selected magnetic field lines overplotted on the AIA 304 Å image. The field lies are calculated using the the potential-field source-surface (PFSS) model (Schatten et al. 1969; Altschuler and Newkirk 1969), which is more suitable for large-scale magnetic structure as in this case. The boundary between the closed field lines (white) and the open field lines (green) corresponds to where the fan surface is attached to the photosphere and also to the location of the CR. Lim et al. (2017) divided the large CR into many smaller sections and examined the local lightcurves of EUV emission within each section to collect the maximum intensity time in each local lightcurve. The collection of the local intensities in the sections is plotted in Fig. 6f along with the time when the location of intensity maximum is read. These are overplotted in green over the time-distance map. A linear fit to the intensity-peak-time gives 161 km s^{-1}, which corresponds to the speed of successive brightenings in the clockwise direction starting from the nearest position to the flaring sunspots. This CRF also shows the radial contraction and expansion in the northern and the southern part, respectively, but at speeds of $\leq$10 km s^{-1}, much lower than the rotational slipping motion.

4.2 Null current parallel to fan surface

We often see an expanding motion of CR in CRFs in addition to the slipping motion along CR as the flare proceeds. We tend to regard this motion as analogous to two-ribbon separation motion in PRFs. However, the IR also expands or moves in position, which is not readily understandable with the 2D picture (Fig. 2). We rather argue that the rapid evolution of the IR provides the rotational motion of the inner spine to cause current to build up over the fan surface. The closest mode to this case is the 3D null reconnection with the current directed parallel to the fan surface, as shown in Fig. 7a–c. Reconnection in the presence of null current parallel to the fan is known to resemble the 2D reconnection, in that the magnetic flux is transported across the separatrix surface in the ideal region (Pontin 2011).

Figure 7d–g shows a CRF at early (Fig. 7d, f) and late (Fig. 7e, g) times. Using the NLFFF model, one can show that the CR, or equivalently, the open–closed field boundary, expands with time (Lee et al. 2016b, a). IR has a finite length and width, which already implies the presence of QSL in the corona (note that IR is a topologically special element). In order to trace the IRs, we plot the negative 304 Å images to emphasize the ribbons at the two stages: 02:59 UT and 04:05 UT. The green contours

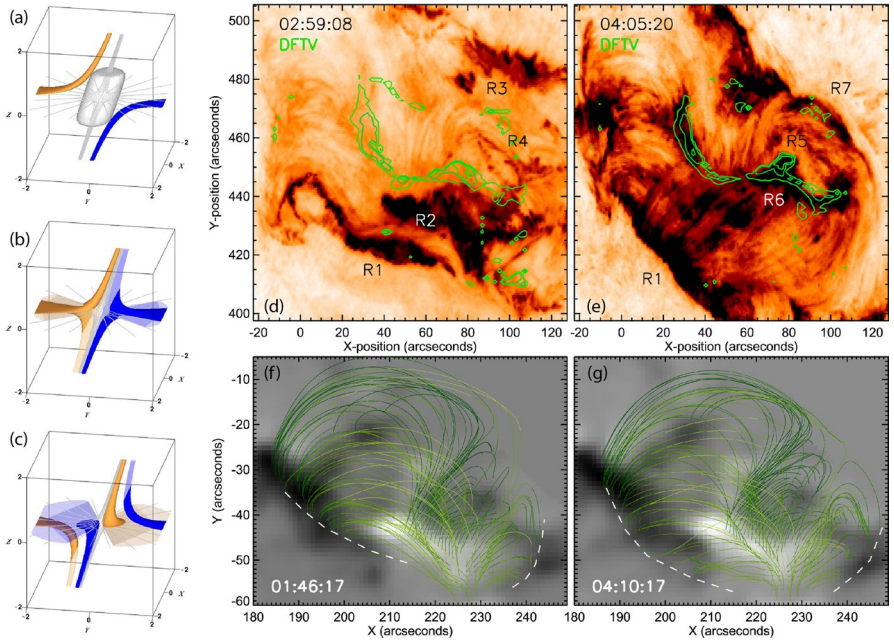

Fig. 7 Torsional fan reconnection. In the theoretical model (**a**–**c**), two flux tubes come into a localized diffusion region (gray surface) around the null, reconnect to each other, and expand (transparent surfaces) after passing through the diffusion region. (Source: Pontin 2011). In an observational example, the 2012-03-27 flare (**d**–**g**), such a connectivity change appears as evolutionary expansion of both IR and CR shown as the DFTV (green contours) on the negative 304 Å images (**d**, **e**). Perspective views of selective field lines extrapolated from the common locations of IR are plotted on the SDO/HMI magnetograms, along with the CR boundary (white dashed lines) (**f**, **g**). Source: Lee et al. (2016b)

represent so-called differential flux tube volume (DFTV), which is a measure for how rapidly field lines are locally squashed (Büchner 2006). This quantity was calculated using the NLFFF model by Wiegelmann (2004) from the HMI magnetogram at the nearest times. In Fig. 7d, the inner ribbon, R2, moves northward to approach another inner ribbon, R4. Both R2 and R4 do not match the high DFTV region in position, which implies that they are not directly connected to the QSL at this time. In Fig. 7e, R2 merges with R4 at the location of the enhanced DFTV region (green contours), after which the ribbons can no longer move north-south, and instead evolve along a more complicated path extending to east–west. The path of this inner ribbon can be regarded as one piece of evidence for the 3D null-point reconnection with the fanward current. The IR expands like the outer ribbons, which has no analogy to the PR motion (Sect. 2).

In the meantime, the outer ribbons, R1–R3–R7, that define the open-closed field boundary significantly advanced in location, implying that the overall fan-dome structure expanded in size and changed its shape overall. Such an idea is supported by the field extrapolation result shown in Fig. 7f, g. The selective field lines are extrapolated from the common locations around the DFTV of two HMI vector magnetograms at times corresponding to Fig. 7d, e. The fan-dome structure is indeed enlarged in response to the complex evolution of IR. As aforementioned (Sect. 2 and Fig. 2) the expansion of CR itself is analogous to the separation of PRs. However, the standard 2D model cannot explain why IR also expands instead of shrinking itself, for which we need the 3D kinematic model with the currents spread over the fan (Fig. 7a–c).

4.3 Torsional null-point reconnection

The above two processes occur in response to the driving torque supplied either by CR (resulting in torsional spine reconnection) or by IR (torsional fan reconnection). When both drivers work together, a current layer may form at the null by a local collapse of both the spine and fan field toward each other, spanning both of them, as depicted in Pontin (2012). The disturbances propagate toward the symmetric 3D null points like Alfvén waves, analogous those in 2D X-point reconnection (McLaughlin et al. 2011). Under the hyperbolic geometry of the magnetic field, the current is intensified until the length scales perpendicular to the spine or fan become short enough to make diffusion important. This self-focusing process consists of rotations and shearing to further increase the degrees of freedom in the system.

Observational detection of the torsional null-point reconnection will be more difficult than the above two cases, because the twisting motion of magnetic field is confined to a smaller coronal region. It is that the current intensifies as the length scales perpendicular to the spine or fan become shorter until the diffusion becomes important. Few radiative emissions, other than microwaves produced by synchrotron radiation, are sensitive to both the strength and orientation of the coronal magnetic field (Lee et al. 1998, 2020b; Lee 2007). Another technical difficulty is that EUV intensities in an intense flaring region are often saturated at observation, making it hard to detect subtle oscillations near spines. Fortunately, currently available microwave instruments show little saturation even in the flare core region.

Lee et al. (2020b) and Lee (2022) presented, for the first time, a detailed microwave observation of the CRF, SOL2014-12-17T04:51, expecting that any oscillatory behaviors in the microwave time profiles should evidence torsional reconnection if present. The target active region has a clear dome-shaped structure in EUV images (Fig. 8b) and quasi-periodic pulsations (QPPs) during this flare have been already studied by Chen et al. (2019) in many wavelengths. Some of their results are plotted in the right hand side of Fig. 8. Lee et al. (2020b) set four local regions on the inverted microwave map (Fig. 8a), and constructed the spatially revolved lightcurves in total intensity (Fig. 8c) and polarized intensity (Fig. 8d) separately. The time profiles indeed show quasi-periodic peaks, which vary with location (Fig. 8a) and polarization states (Fig. 8c, d). Initially the oscillation of total intensity was

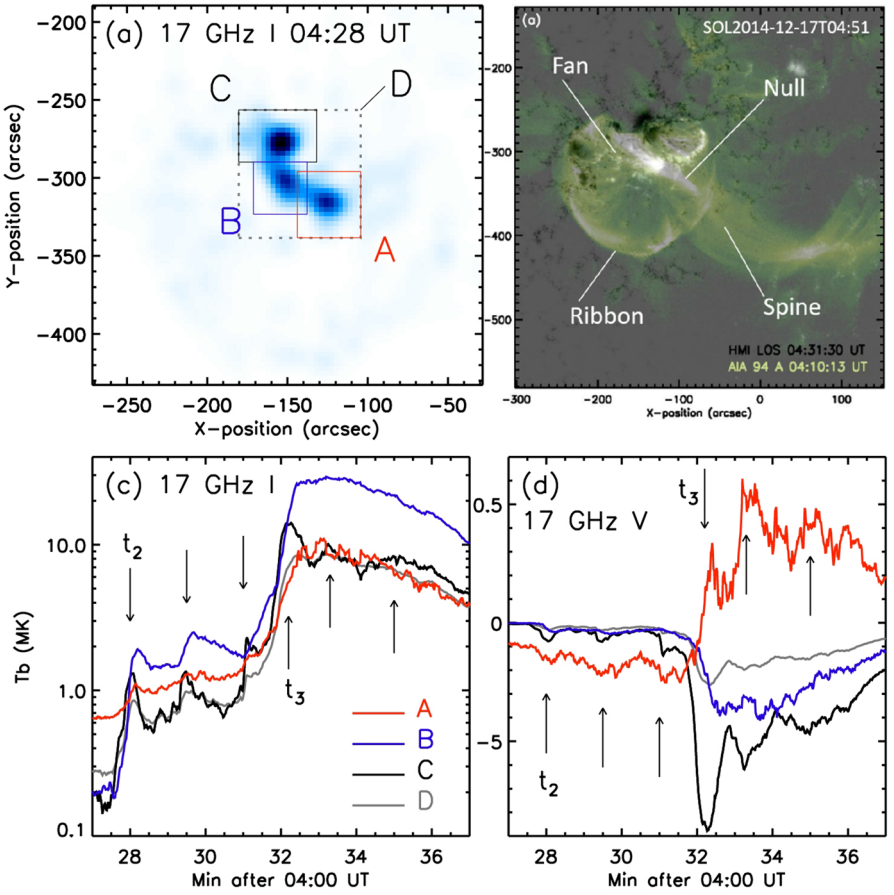

Fig. 8 An observational example of torsional null-point reconnection. The SOL2014-12-17T04:51 flare from NOAA AR 2242 is shown as an inverted NoRH 17 GHz map (**a**) and AIA 94 Å intensity map over the HMI magnetogram (**b**). Local lightcurves of total (**c**) and polarized (**d**) intensities calculated from the four local regions, A–D, marked in (**a**) show multiple peaks indicated by the vertical arrows. Source: Lee et al. (2020b)

more obvious and located in the outskirt of the active region. On and after the flare, the oscillation of the polarized intensity dominates in the location close to the IR and thus the spine, consistent with the theoretical finding that the rotational motions around the null are analogous to the Alfvén waves propagating toward 2D X-points (McLaughlin et al. 2011). This thus gives a potential piece of evidence for the torsional null-point reconnection around the 3D null.

The quasi-periods may provide another piece of information on the torsional mode of reconnection. The microwave time profiles show the quasi-periods about 1–2 min (Lee et al. 2020b), whereas analysis of the EUV and UV data gives 3–4 min in the outskirts of the active region (Chen et al. 2019). It is likely that the relative longer periods in the outskirts of the active region near CR would belong to the torsional fan oscillation and the shorter period found close to IR, to the torsional spine reconnection. In that case, they would represent shearing motion and rotational motion of the magnetic field, respectively. The positional shift of the dominant oscillation from the CR toward the IR found in Lee et al. (2020b) and Lee (2022) is also reminiscent of the torsional waves moving toward the null from an ideal region (Rickard and Titov 1996; Pontin and Galsgaard 2007) and also those propagating along the outer spine after reconnection (Wyper et al. 2017). This finding of oscillatory microwave peaks in the core of the CRF should provide an important clue to the torsional null reconnection theory, because no other observational tools are available to detect such changes associated with rotation and shearing of magnetic field at this scale and location.

4.4 Spine-fan reconnection

Spine-fan reconnection mode may be a more common type of reconnection occurring in a spine-fan structure. First of all, the magnetic structure is most suitable for hosting the spine-fan reconnection. Second, although spine-fan reconnection also requires a driving force for initiation, the driver may not necessarily be an organized rotational driving motion needed for the torsional reconnection modes as discussed above. In Sect. 3.2.3 we have discussed a few properties of fan-spine reconnection to some degree of approximation. In more detail, however, the spine-fan reconnection would occur within a current sheet localized in all 3D around the null, and the current sheet is formed by a local collapse of the fan and the spine field when a shear disturbance of either the spine or the fan occurs (Pontin and Galsgaard 2007; Galsgaard and Pontin 2011). Here we focus on such asymmetric current distribution which is missing in our formulation.

Figure 9 reproduces a result of the resistive MHD simulation for spine-fan reconnection performed by Pontin et al. (2013) and Hα observations of a CRF (Wang and Liu 2012) for a comparison. In the simulation, a bipole magnetic field is set with an embedded parasitic polarity and a coronal null point above it, and the system evolves as a result of imposing a surface motion toward the parasitic polarity. From top to bottom of Fig. 9a, we can see that a current front forms and propagates upward and focuses on the separatrix surface around the null point, and then dissipates out after the driving ceases. We draw attention to the current layer that is more inflated in one

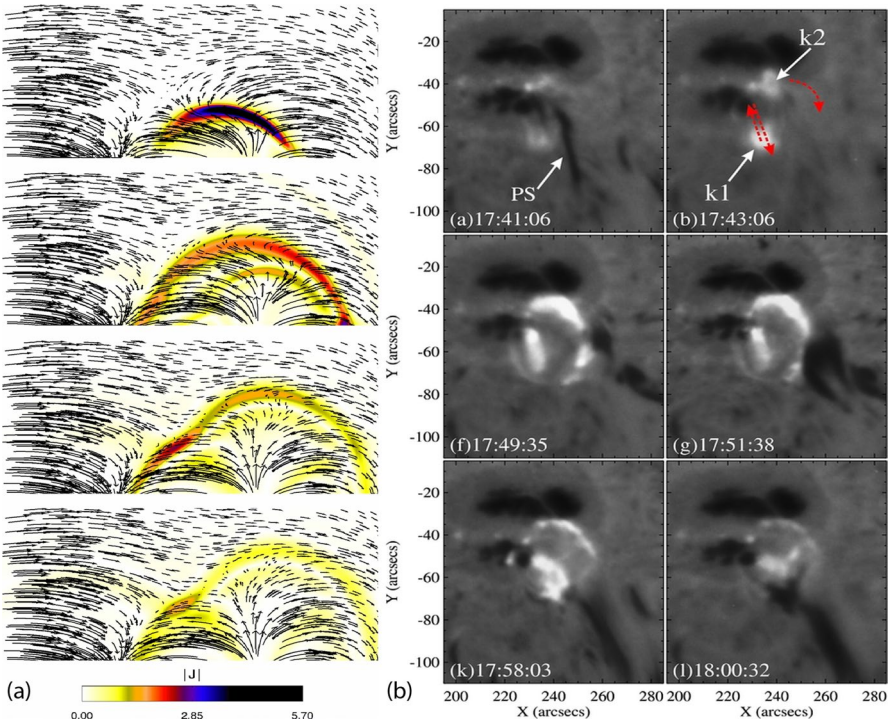

Fig. 9 Spine-fan reconnection, MHD simulation vs. observation. **a** From top to bottom, the frames show the magnetic field (arrows) and current density (shading) evolving with time in the x–z plane. Source: Pontin et al. 2013. **b** Hα-0.6 Å images of the 1991-March-17 flare are shown with the motions of the central ribbon (k1) and the outer CR (k2) marked by red arrows. PS stands for the preflare surge. Source: Wang and Liu 2012

side than in the other. This thickness variation, when projected on the surface, manifests itself as ribbon contraction on one side and expansion on the other. In terms of position, the footpoint locations of field lines initially lying under the dome end up outside the dome after the reconnection and those beginning outside the dome end up inside the CR.

Figure 9b displays an event among the very first reported CRFs seen in the Hα line (Wang and Liu 2012). We suggest the spine-fan reconnection for this event because the CR grows asymmetrically to be thicker on the right hand side and thinner on the other side. Authors emphasized the asymmetric kernel motions too. The kernel, k1, first moves northeastward at $\sim$ 40 km s^{-1}, and k2 shows a sequential brightening in the clockwise direction at $\sim$ 100 km s^{-1}. Such an asymmetric CR motion is seen in virtually all six CRFs that they studied. There can be many reasons as to why the whole CR ribbon may not brighten up simultaneously. Either non-uniformity of field at photosphere around CR or preferential acceleration of particles in certain directions in a fan-spine configuration (e.g. Baumann et al. 2013; Pallister et al. 2021). It has been demonstrated that the dimensions of the diffusion region and

reconnection rate are strongly dependent on the degree of symmetry of the initial null point field (Al-Hachami and Pontin 2010). While it is challenging to check the asymmetric kernel dynamics against all these possibilities, (Wang and Liu 2012) simply calculated a flux transfer rate from the difference of ribbon fluxs before and after the flare as high as $\dot{\Phi} \approx 6 - 20 \times 10^{18}$ Mx $\cdot$ s^{-1}, which is largely determined by the relative areal change of the ribbons and their asymmetric motions.

We present another example for spine-fan reconnection in Fig. 10a, b together with a schematic illustration in Fig. 10c, which may be more obvious from a macroscopic viewpoint. In contrast to the above case where a slow surface flow drives the current to build up in the separatrix, the sun may provide an external macroscopic driver. It is rather common that filaments reside elsewhere, either inside or outside the circular dome. A filament unstable to any ideal MHD instability may erupt to perturb the overlying fan-spine structure. In our proposition, interaction of flux ropes residing near both the fan and spine may also incur the spine-fan reconnection. In this line, Browning et al. (2008) and Hood et al. (2009) have studied the formation of current layers and subsequent energy release following the onset of the kink instability in a straight, line-tied flux tube in resistive MHD simulations. In addition, numerical modeling of the loss of stability of curved flux ropes, to either the kink (Kliem et al. 2004) or torus (Kliem and Török 2006) instability, has implicated reconnection at a current sheet in a QSL beneath the flux rope as facilitating the subsequent eruption.

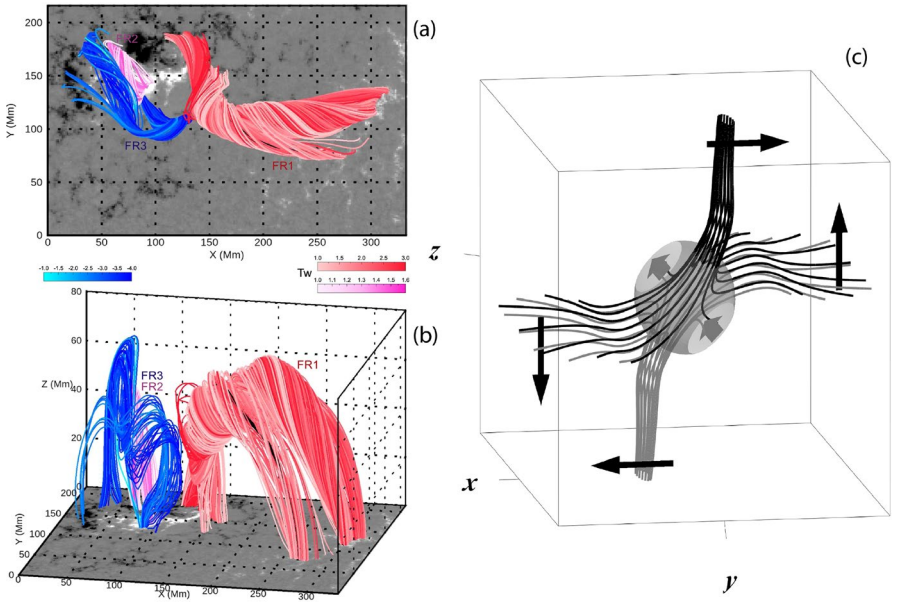

Fig. 10 Another example for spine-fan reconnection. The left panels show the NLFFF lines at 04:07:54 UT before the SOL2014-12-17T04:51 flare in the top-down view (**a**) and in a 3D perspective view (**b**). The field lines colored according to the twist number show three flux ropes distinguished by different color tables for their twist numbers. Source: Liu et al. 2019. The right panel shows a theoretical idea presented with magnetic field lines (black and gray lines), a current density isosurface (shaded surface), the current flow (gray arrows), and driving plasma (black arrows). Source: Pontin 2011

In Fig. 10a, b three flux ropes are interacting around the fan surface. The longest one denoted as FR3 actually runs close to outer spine connecting the active region flux to the outer ribbon. FR2 mostly runs along the fan. FR1 is a small filament that grows within the fan. FR2 and FR3 have magnetic twist in the opposite sense (represented by the blue/red colors), and are more vulnerable to reconnection. In view of the flaring timeline presented by this work (Liu et al. 2019), FR1 erupted either due to its instability or to emerging flux from below. The eruption of FR1 subsequently triggered the reconnection between FR2 and FR3, which resembles the spine-fan reconnection depicted in Fig. 10c. We believe that this type of reconnection resembling the spine-fan reconnection can be viewed as a loop-loop interaction which is common in solar flares.

4.5 Hybrid nature of CRFs

In some CRFs, an eruptive filament is embedded along the PIL under the fan dome. When it erupts it should affect the null point on its way out. Whether the null point reconnection leads to the filament eruption (Sun et al. 2013) or the erupting filament presses on the null point to trigger the reconnection is not known (Jiang et al. 2014; Zhang et al. 2015; Joshi et al. 2015). If the filament successfully erupts, it may leave a pair of PRs, and as a consequence, we will see PR and CR coexisting together. This hybrid nature has been reported in many papers, since the start of the CRF study (Masson et al. 2009, 2017; Wang and Liu 2012; Sun et al. 2013). All of these papers presented an illustrative picture like the one reproduced in Fig. 11. The events shown in Figs. 12, 13 may also belong to this category. Although this phenomenon is not exactly in any of the above categories, it certainly deserves attention how the filament eruption affects the subsequent evolution of the fan-spine system.

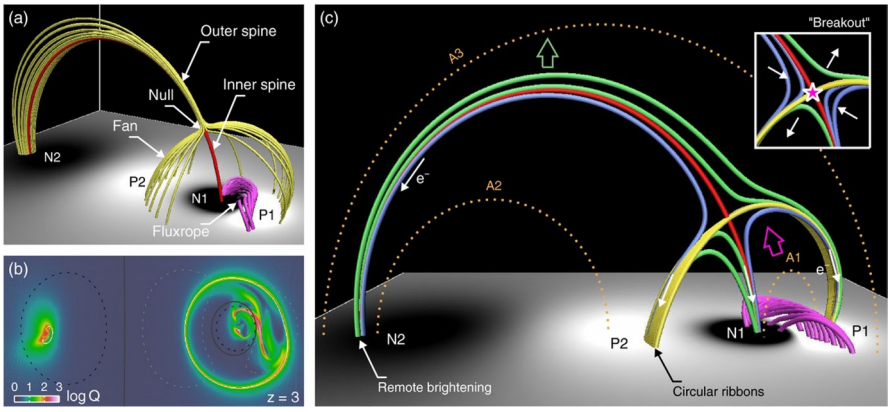

Fig. 11 Skeleton representation of a typical CRF based on the NLFFF model. **a** Four flux patches, P1/N1 and P2/N2, at the lower boundary are shown along with a null point above N1, a flux rope (pink), the spine (red) and the fan (yellow). **b** A squashing factor map on a *xy* plane shows the QSL footprint. **c** 2D representation of the system illustrates possible slippage within the fan QSL (yellow) and breakout-type reconnection (inset) round the null. Source: Sun et al. 2013

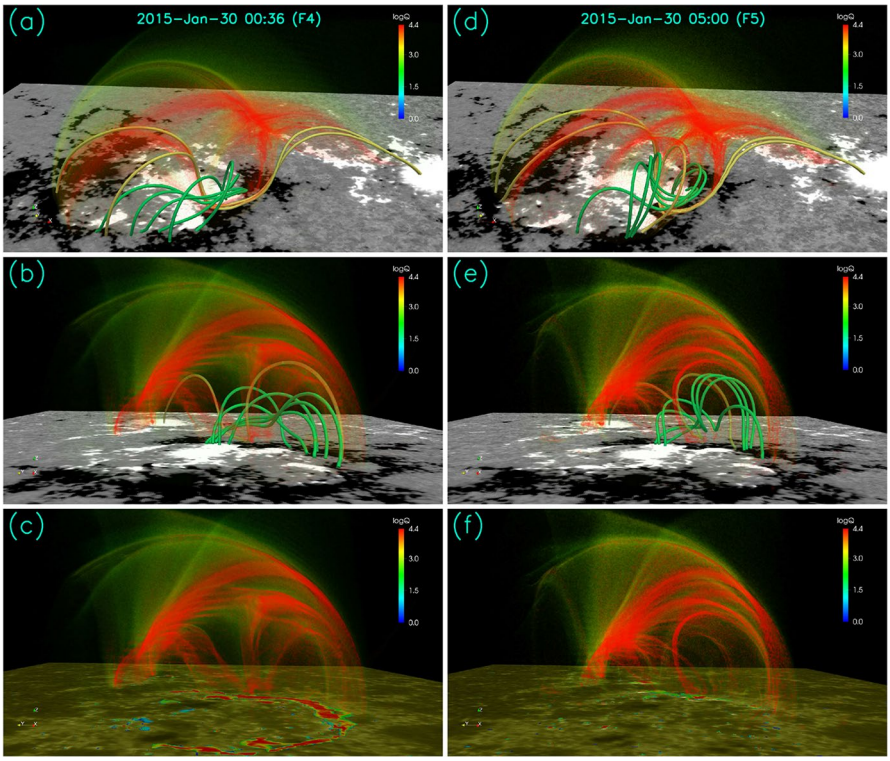

Fig. 12 A hybrid structure in two flares, F4 (**a**–**c**) and F5 (**d**–**f**). The QSLs calculated from the NLFFF are rendered as transparent surfaces scaled according to log Q. The two sets of field lines: the magnetic flux rope (yellow lines) and field lines within the dome-like QSL (green lines) are plotted over the SDO/HMI magnetogram (**a**, **b**) and the SDO/AIA 1600 Å image (**c**) at different viewing angles. The same for (**d**–**f**). Source: Zhong et al. (2019)

Sun et al. (2013) presented a complete topological picture of a CRF in their study of hot coronal loops connecting a circular chromospheric ribbon and a remote brightening in the 2011-11-15 flare, and found that these loops partly trace the evolving spine field line. Mandrini et al. (2014) analyzed activities and brightenings closely associated with the confined 2010 November 11 C4.7 circular-ribbon flare, and suggested that only a complete topological analysis including QSLs can explain the flare ribbon locations. Indeed, overlap between flare ribbons and QSLs from NLFFF models have been reported in circular-ribbon flares (Janvier et al. 2016; Jiang et al. 2016) and also the more standard two-ribbon flares (Janvier et al. 2016; Zhang et al. 2015; Liu et al. 2014).

An interesting aspect of hybrid CRFs is that an erupting filament can also trigger current sheet formation and 3D reconnection as an external driver with nulls present or absent. This is reminiscent of the non-null reconnection mode (Pontin 2011, 2012) where FR plays a role in triggering the formation of a current sheet. Such filament eruption within the closed fan may occur under ideal MHD instabilities, e.g.

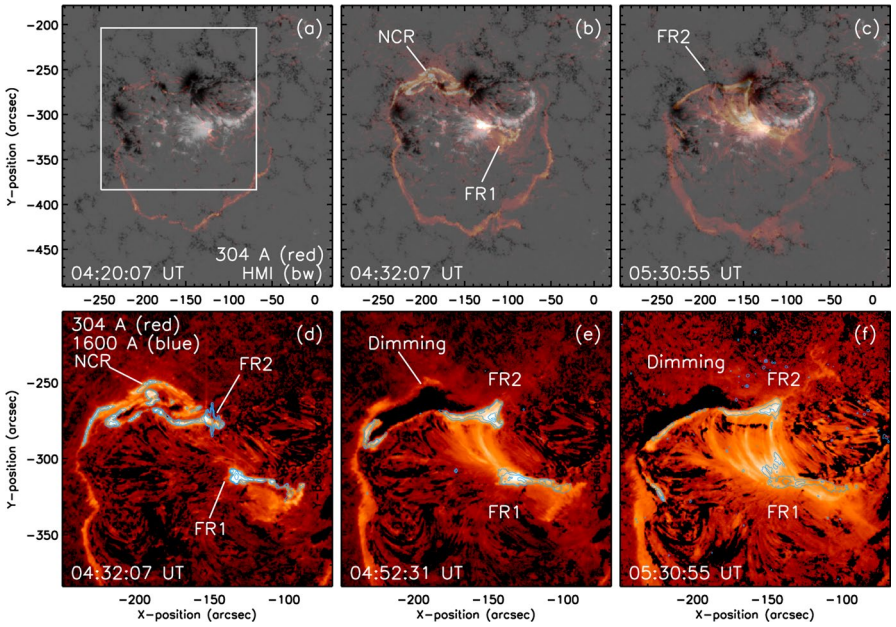

Fig. 13 Coexistent PRs and CRs at three times during the SOL2014-12-17T04:51 flare. The AIA 304 Å intensities rendered transparent over the HMI longitudinal magnetograms (**a**–**c**) show the entire CR evolution through the flare. Zoomed-in views (white box) of the 1600 Å intensity (contours) over the 304 Å images (**d**–**f**) show the evolution of the northern CR (NCR) and two PRs (FR1 and FR2). NCR in the preflare phase (**d**) is annihilated leaving a dimming region (**e**, **f**). Source: Lee et al. (2020a)

kink and torus instabilities (Lee et al. 2016a; Li et al. 2018b; Liu et al. 2019; Mishra et al. 2021; Howson et al. 2021). Not only the resistive reconnection but the ideal MHD instabilities should therefore be integrated into the 3D null reconnection in a fan-spine structure.

4.6 Transformation of 3D to 2D reconnection

Once a solar filament is admitted as an indispensable element to the mechanism of solar 3D reconnection, we may ask to ourselves what is the consequence of the eruption staring from inside of a closed fan surface. This question did not arise in the 2D standard model because such a filament lies above the X-point (see Fig. 3g) and its eruption needs not destroy the X-point underneath. The eruption may induce or enhance the X-point reconnection or create a current sheet behind itself, but it can otherwise proceed freely along the open field. The upward motion of the filament naturally maintains the X-point configuration forming the so-called standard model for solar eruptive flares. On the other hand, CRFs have a confined structure, a filament starting inside the closed fan will need to break out the fan-spine structure causing more complicated structural changes. A possible consequence of the break-out eruption is that 3D null reconnection is followed by the two quasi-parallel

ribbons forming behind the erupting flux rope, and thus by 2D reconnection (Zhong et al. 2019; Joshi et al. 2021; Lee et al. 2017, 2018, 2020a, b). Slipping motion of the substructures preceding major eruption (Li et al. 2018) may also be considered in this category.

Zhong et al. (2019) proposed a transformation of topological structure from that of one CR to three PRs during multiple flares based on Hα and ultraviolet images along with the NLFFF models. At first, sheared arcades under the dome-shaped fan surface develop into a flux rope through magnetic reconnection to produce a CRF. Subsequently, the flux rope bifurcated to form the three PRs. They identified the bifurcation of the flux rope as the main factor for the transition from CRF to PRFs. Figure 12 shows snapshots from the model constructed by Zhong et al. (2019) showing the transition from CRF to a set of PRFs. The QSLs calculated from the NLFFF are visualized as the transparent layers colored according to the squashing factor ranging form green ($\log Q = 2.0$) to red ($\log Q = 4.4$). The maps of $\log Q$ distribution show a large dome-shaped QSL induced by the quadrupolar-like magnetic field, and a torus QSL surrounding the flux rope. The yellow field lines represent the bifurcated portion of the magnetic flux rope and the green lines lie within the large-scale QSL. It is claimed that due to the existence of the magnetic flux rope, the semicircular-shaped negative polarity is separated into two parts.

Lee et al. (2020a) present another case of subtle change of a CR associated with formation of PRs out of a CR. Figure 13 shows the CRF, SOL2014-12-17T04:51, in the 304 Å image over the HMI longitudinal magnetograms (top panels) and the 1600 Å intensity over the 304 Å images at three times from preflare to postflare. The CR in the south (13a) is narrow and becomes wider with time (13b, c). The CR in the north (NCR) is initially very faint (13a), but maximally expanded northward in the flare maximum (13b). In the late phase (13c), another PR (FR2) seemingly conjugate to FR1 appears in the south of the previous location of NCR. During the flare, FR2 approaches NCR, and later NCR disappears and only FR2 is left (13e). The area between NCR and FR2 on the 304 Å images is now dim, which implies that the closed fan fields rooted between NCR and FR2 open up and are consequently disconnected from the active reconnection site. In effect, FR2 merged with the new NCR, and the old fan surface in the dimming region is annihilated and a new fan surface formed in a reduced size.

The above-demonstrated transformation of CRF to PRF brings up a couple of questions: is there a counter example, i.e transformation of PRs to CRs? If not, PRF would be the ultimate mechanism for solar eruption and the fan-spine structure suitable for CRFs may be so fragile as not to allow multiple episodes of reconnection or eruption. There can, of course, be cases where a filament inside the dome-shaped fan erupts, but fails to break out, at least initially. Wang and Liu (2012) showed that homologous jets from CRFs are possible. Li et al. (2019) studied two types of confined flares, which demonstrates that such a failed eruption may occur depending on the instability condition for filaments and the nonpotentiality of the field around. Alternative explanation for the partial brightening of a CR ribbon includes non-uniformity of magnetic field along the CR and preferential acceleration of particles in certain directions in such a configuration (e.g., Baumann et al. 2013; Pallister et al.

2021). These works highlight the complexity of triggering reconnection in solar 3D fan-spine structure.

5 Magnetic reconnection in arcade structure

Ever since the first quantitative model of magnetic reconnection was presented by Sweet (1958) and Parker (1957) and later by Petschek (1964) , physics of reconnection has been studied in 2D geometry with the main focus on the dimensionless reconnection rate (Sect. 3.4). Solar flares often occur in a magnetic arcade structure, which can be approximated to a 2D structure across the arcade axis, by which many observational properties of PRFs could be explained. This established the standard model for solar eruptive flares, also known as the CSHKP model (Aulanier et al. 2012). Strictly speaking, the projection of the coronal 2D structure on the photosphere should appear as 1D structure, and the reconnection rate given by a ribbon speed and local magnetic field (Table 1) has served as a main observable quantity. On the contrary, solar flare ribbons exhibit variability of brightness and speed along the ribbon length and their finite area often contains many fine structures, which are not directly compatible with the 2D X-point reconnection model. These anomalies suggest new challenges still remaining in the 2D standard framework. Solar 2D magnetic reconnection forms a huge area of research. Instead of an extensive review, we thus focus on selective issues of 2D reconnection that may shed light into the effect of dimensionality on reconnection physics.

5.1 Discrete ribbon motion in 1D

The reconnecting current sheet may undergo fast variation in time and space. We thus need both high spatial resolution and high time resolution to explore such physics which is otherwise smoothed out in detection. In practice, a higher resolution brings up more complex morphology, and a higher time cadence temporal overlaps in ribbon areas. Both issues make it hard to define ribbon dynamics. In order to overcome these conflicting requirements we may want to decompose an irregularly shaped ribbon into a total area and a center-of-mass position, which enables defining the fine-scale 1-D motion. This effectively reduces the ribbon dynamics from 2D to 1D so that we can focus on the original 2D reconnection physics.

Lee et al. (2006) carried out such an analysis to get the results shown in Fig. 14. They used an extremely fast Hα camera available in Big Bear Solar Observatory (BBSO) to determine the center-of-mass location of the flare kernel in a moderate flare. They marked, over a Michelson Doppler Imager (MDI) magnetogram (gray-scale), the center-of-mass locations with colored dots (Fig. 14a). The time-stamped point distribution already suggests that the ribbon motion is not uniform but rather stepwise. Note that the individual flare ribbon area is much wider than the concentration of the points and also has an irregular shape each time. The time-stamped point distribution concentrated within a narrow region signifies that the ribbon is more or less stationary in that region; gaps between groups of concentrated points

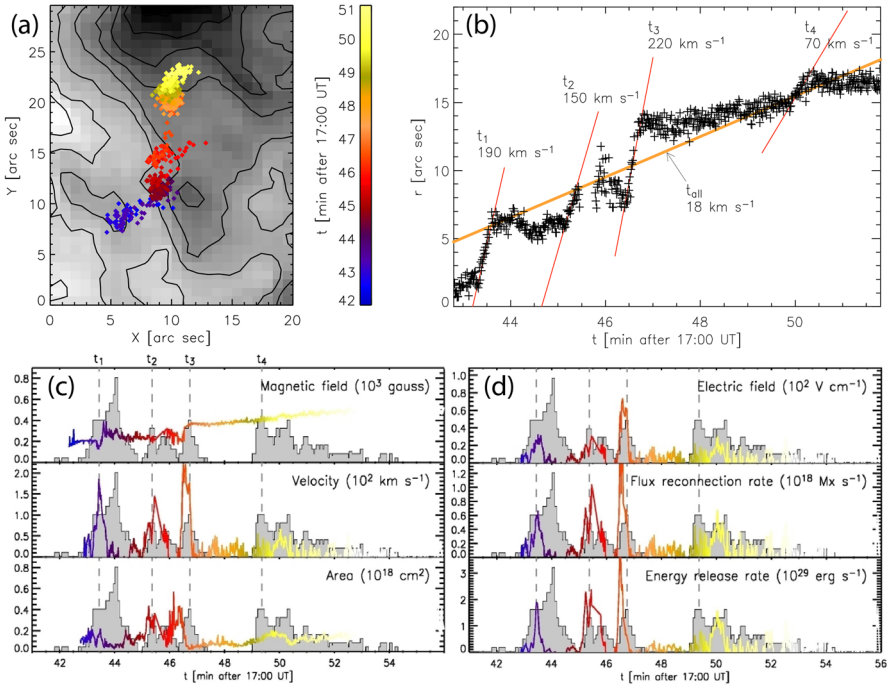

Fig. 14 Discrete 1D motion of a PR for 2D reconnection during the 2002 September 9 flare. **a** Location of the Hα blue-wing ribbon center (colored dots) overlaid on the MDI magnetogram (gray scale). **b** 1D distance of the ribbon as a function of time showing stepwise increase at the four time intervals marked with red guide lines along with the inferred speeds. **c** Observed reconnection parameters: local magnetic field strength, ribbon velocity, and area. **d** Derived reconnection parameters: electric field, flux reconnection rate, and energy release rate. The gray histogram in each panel shows the RHESSI count rate at 25–50 keV for comparison with the discrete reconnection. Source: Lee et al. 2006

correspond to the locations where the ribbon speeds up at the enhanced magnetic reconnection rate.

The stepwise motion of the ribbon is more clearly seen in Fig. 14b where the location of the ribbon (cross symbols) is shown as a function of time together with the solid guide lines showing the speed determined at selected time intervals. The first stepwise motion, for instance, occurs around ~ 17:43:30 UT at which time the ribbon is advancing about ~ 5″ in ~20 s achieving the speed ~ 160 km s^{-1} (see the solid guide lines indicating the speed). Other stepwise motions also incur high velocities ranging 60–220 km s^{-1}, which are much higher than the typically reported ribbon velocity, a few tens of km s^{-1} (Jing et al. 2007). In order to check why such an enormously different result is obtained in the present case, we made another fit to the average motion over the whole period of the flare activity. If we count the distance after 17:43:30 UT, the total distance traveled is ~ 10″ in ~7 min, and the overall speed is only ~18 km s^{-1} (shown by the thick guide line marked as $t_{\rm all}$), in agreement with the above-mentioned typical speed.

Use of such data of ribbon area and 1D speed together with local magnetic field allowed them to determine various quantities shown in Fig. 14c, d. The observed parameters of the 2D magnetic reconnection: local magnetic field strength, ribbon velocity, and area are shown in Fig. 14c, and the derived parameters of the 2D magnetic reconnection: electric field, flux reconnection rate [Eq. (4)], and energy conversion rate [Eq. (8)] are shown in Fig. 14d. The derived quantities also show the stepwise variation like the ribbon motion (Fig. 14b) and coincide with the multiple peaks of 25–50 keV hard X-rays observed with the Ramaty High-Energy Solar Spectroscopic Imager (RHESSI) shown as a gray filled histogram in each panel. Since the hard X-ray flux is an independent measure for the energy release, the derived quantities represent an episodic variation of the magnetic reconnection and energy conversion rates.

Therefore reducing the dimension of the dynamics from 2D to 1D using the center of mass representation of the ribbons allowed us to focus on the fine time structure of the 2D X-point reconnection more clearly. In view of the contrasting temporal variations of magnetic field and that of ribbon speed shown in Fig. 14c, it is not the local field strength but the ribbon motion that indicates the discrete reconnection rate in the corona. In the interpretation of Lee et al. (2006), the stepwise variation of the ribbon motion should represent a pulsating current sheet as a self-organizing process of the current and its area. A supporting theoretical model was independently presented by Kliem et al. (2000).

5.2 Structure along ribbon axis as 2D process

The 2D X-point model can accommodate some of the nonuniform structures along the ribbon axis and each X-point lined up along a ribbon is treated independent of each other. Asai et al. (2004) provided an explanation of the puzzle as to why hard X-ray sources appear in isolated concentrations whereas Hα ribbons in a continuous distribution. Their argument is based on the Petschek model (Petschek 1964) in which the dimensionless reconnection rate, M, is insensitive to the local magnetic field. In this case, the inflow, v_i, should be proportional to the field strength to cancel out the dependence of the reconnection outflow, the Alfvén speed, on the magnetic field. The energy conversion rate [Eq. (5)] is then as sensitive to the magnetic field as $\sim B^3$. In this case the limited sensitivity of hard X-ray instruments can make the hard X-ray sources mainly appear in strong field regions, which explains why ribbons are seen in Hα but not in hard X-rays.

This idea motivated a few follow-up studies to check discrete hard X-ray sources against continuous Hα ribbons in position, motion, and brightness (Jing et al. 2007; Lee and Gary 2008). They were able to demonstrate that the spatial distribution of the hard X-ray intensity can be explicable if local field strength variation along the ribbon front is incorporated into the calculation of the reconnection rate and energy conversion rate [Eqs. (4, 8)]. Such result implies that some variability along Hα ribbons can be understood in terms of an inhomogeneous set of 2D X-point configuration, but is insufficient to fully resolve the puzzle as to why hard X-ray sources never appear in a distribution as continuous as Hα flare ribbons.

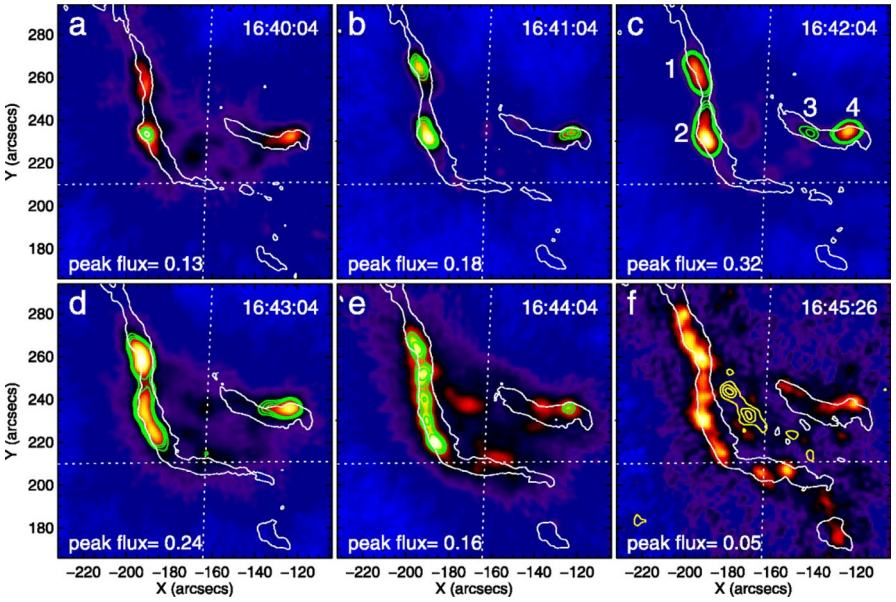

Fig. 15 Unusual hard X-ray ribbons. Time sequence of RHESSI hard X-ray images during the 2005-05-13 flare reconstructed with 5.9″ arcsec FWHM resolution. **a**–**e** show 25–50 keV maps with the peak flux labeled in each panel and the green contours at levels of 0.1, 0.115, and 0.13 photons cm^{-2} s^{-1} $arcsec^{-2}$. **f** shows 6–12 keV map and yellow contours at levels of 50%, 70%, and 90% of its maximum flux. The white contours outline the TRACE 1600 Å ribbons taken at the middle of each RHESSI time interval. Source: Liu et al. (2007)

Liu et al. (2007), for the first time, demonstrated that even hard X-ray sources may appear in the form of ribbons depending on the amount of energy released via reconnection. Figure 15 shows rather unique images of unusual ribbon-like hard X-rays at energies as high as 25–100 keV, which show the apparent inconsistency between hard X-ray and Hα morphology was simply due to the finite sensitivity limit of hard X-ray instruments and faint X-ray emission between the regions of intense concentration of energy deposition is not detected unlike Hα emissions. Liu et al. (2008) further investigated the local HXR spectrum determined using the hard X-ray imaging spectroscopy to find an anticorrelation between the HXR spectral index and the local electric field along the ribbon, which suggests nonthermal electron acceleration by the electric field during flares. Both studies therefore reached the same conclusion that the 3D reconnection structure in some cases can be approximated by a stack of 2D standard reconnection models along the ribbon.

With improvements in spatial resolution, time cadence, and sensitivity, detailed structure of flare ribbons has been a target of active research. Jing et al. (2016) used exceptionally high resolution Hα images from the Visible Imaging Spectrometer installed at the Goode Solar Telescope (GST, Goode and Cao 2012) in BBSO to measure the fine structures (below 500 km) of flares, which may reflect the complex structure of the reconnecting current sheet. French et al. (2021) analyzed the high-cadence (1.7 s) data of the Interface Region Imaging Spectrograph (IRIS) slit Jaw

Imager to probe for the growth and evolution of key spatial scales along the flare ribbons. Combining analyses of spatial scale growth with Si iv nonthermal velocities, they provided evidence of the tearing mode instability triggering a cascade and inverse cascade toward a power spectrum consistent with plasma turbulence. Naus et al. (2022) reported spatio-temporal evolution of EUV ribbons and hard X-rays in a solar flare in which the reconnecting coronal current sheets, although highly structured, remain quasi-two-dimensional. The magnetic energy release associated with them occurs systematically, rather than stochastically, thus validating the applicability of the standard 2D model to a wider range of solar flare reconnection.

5.3 Structure along ribbon as 3D process

There are other cases of PRFs, which look like 2D reconnection but should be understood as 3D reconnection. Grigis and Benz (2005) reported the RHESSI observations that exhibit continuous motions of double hard X-ray sources which can be regarded as footpoints of magnetic loops. It, however, moves parallel to the PIL, as opposed to the standard model. Qiu et al. (2002) also found a parallel motion along Hα ribbons, which barely correlates with hard X-ray lightcurves. Although such flare kernel motions parallel to the ribbons had often been considered as irrelevant to the reconnection process, a better understanding of this issue was gathered by several MHD simulations designed for a 3D extension of the standard model. They were able to demonstrate that the strong-to-weak shear transition (Aulanier et al. 2012, 2013) and slip-running reconnection (Janvier et al. 2013) can occur during solar flares. In this case, the parallel motion results from a reconnection-driven transfer of the differential magnetic shear, and can be addressed by including a time-dependent guide field to the 2D magnetic arcade structure.

By reanalysing the high-resolution Hα data of Jing et al. (2016), Cannon et al. (2022) found a new phenomenon of sudden acceleration of the ribbon motion around a light bridge. Light bridges are substructures in sunspots that are known to possess different magnetic structures from the other parts of the active region (e.g., Toriumi et al. 2015). In their observation shown in Fig. 16a, an Hα ribbon moves to the left, and the ribbon front in the location of the light bridge runs ahead of the other part of the ribbon, as indicated by the white arrow. Figure 16b shows a zoomed-in view of the region where the enhanced ribbon speeds (10–20 km s^{-1}) are found around the light bridge (blue arrows) and the ribbon front (green line) is approximately parallel to the PIL. The RHESSI observation shows a single hard X-ray source in 50–100 keV located near the region of the enhanced ribbon motion. An NLFFF model reveals that the field lines stemming from a light bridge are connected to a remote region separated from the regions connected to other part of the ribbon. Such a rapid connectivity change may enhance the local reconnection rate and accelerate the ribbon motion around the light bridge. It also suggests that the reconnection inflow at the point would be directed to a different angle implying locally nonzero $\mathbf{E} \cdot \mathbf{B}$ in that location. This is a piece of evidence for a large-scale solar 3D reconnection, which prompts an MHD modeling capable of accommodating a complex coronal field for 3D reconnection.

5.4 Fine structures within ribbons

Solar flare ribbons often exhibit fine structures consisting of multiple kernels and discrete brightness along with their complex structure and temporal variation. The discrete nature of ribbons in hard X-rays were pointed out by Asai et al. (2002, 2004) and Krucker et al. (2003). The randomly orientated motion of isolated brightness within PRs is clearly visible in groups of UV footpoints on TRACE images moving as the flare progresses (Fletcher et al. 2004). When viewed in high-resolution high-cadence Hα images and animation (Jing et al. 2016), it is common to see significant fine structure in the form of wave-like perturbations and hooks. A clear counterclockwise hook motion is visible when the ribbon front exits the light bridge (Fig. 16). These features are not predicted by the simplified 2D model, but might be reproduced by imposing microturbulence around the X-line or the reconnection current sheet.

Brannon et al. (2015) analyzed bright knots and wavelike perturbations in a section of flare ribbon. Aside from wavelike perturbations, spirals are also occasionally observed in flare ribbons. Dudík et al. (2016) studied this event in detail (see also, e.g., Cheng et al. 2015; Li and Zhang 2015; Zhao et al. 2016; Li et al. 2018c) and noted that the hook especially continually evolved wriggled with similar spiral structures. In some studies, these spiral structures are attributed to the Kelvin-Helmholtz instability (Ofman and Thompson 2011), and in later studies these are regarded as a signature of flux rope formation within the current layer. These motions seem to

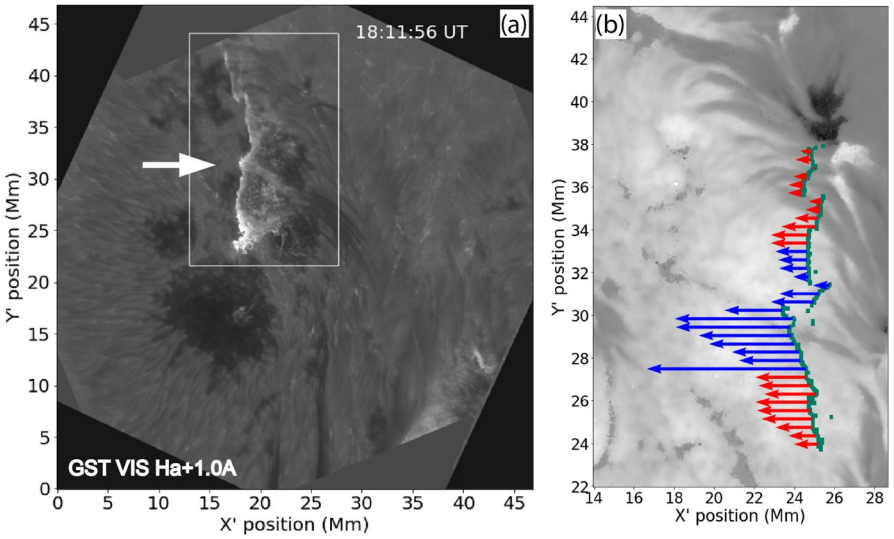

Fig. 16 Fine structure of a solar flare ribbon revealed by the 1.6 m GST in BBSO. **a** The VIS Hα+1.0 Å image shows the ribbon of the 2015-06-22T18:23 flare in NOAA AR 12371 with a light bridge indicated by the white arrow. **b** A zoomed-in view of the image shows the enhanced ribbon speed around the light bridge (blue arrows) and the ribbon front (green line) approximately parallel to the PIL. The enhanced speed ranges between 10 and 20 km/s (Courtesy of B. Cannon et al. 2022). A supplementary movie is available in Jing et al. (2016)

be associated neither with the direction of the large-scale structure nor a large-scale QSL associated with 3D null point structure. Parker and Longcope (2017) attempted to explain these findings based on a quasi-2D tearing analysis involving velocity shear flows.

More recently, Wyper and Pontin (2021) performed a simulation to verify whether these small-scale motions within PRs are related to plasma instability in the reconnection current sheet. They started with an analytical 3D magnetic field representative of an erupting flux rope with a flare current sheet below it, and introduced small-scale flux ropes representative of those formed during a tearing instability in the current layer. They investigated the squashing factor, Q, on the solar surface to identify the shape of the presumed flare ribbons and fine structure. Figure 17 shows part of their results: $\log Q$ for sinistral (a) and dextral (f) flux ropes. Close-up views of the spirals in the small green boxes marked in (a) are shown in (b–e). Similarly, those in the boxes marked in (f) are displayed in (g–j). Some of the close-up views are presented in the right panels with the aspect ratio adjusted to show the small-scale structure in more detail. Arrows show the handedness of the hooks and spirals while the dashed line shows the PIL.

The simulation result shown in Fig. 17 suggests a direct link between the ribbon fine structure and the micro-physics in the flare current sheet. In this simulation, the majority of the ribbon fine structure originates from the oblique tearing modes. Depending upon the size, location, and twist of the small-scale flux ropes, breaking wavelike and spiral features within the hooks and straight sections of the flare ribbon

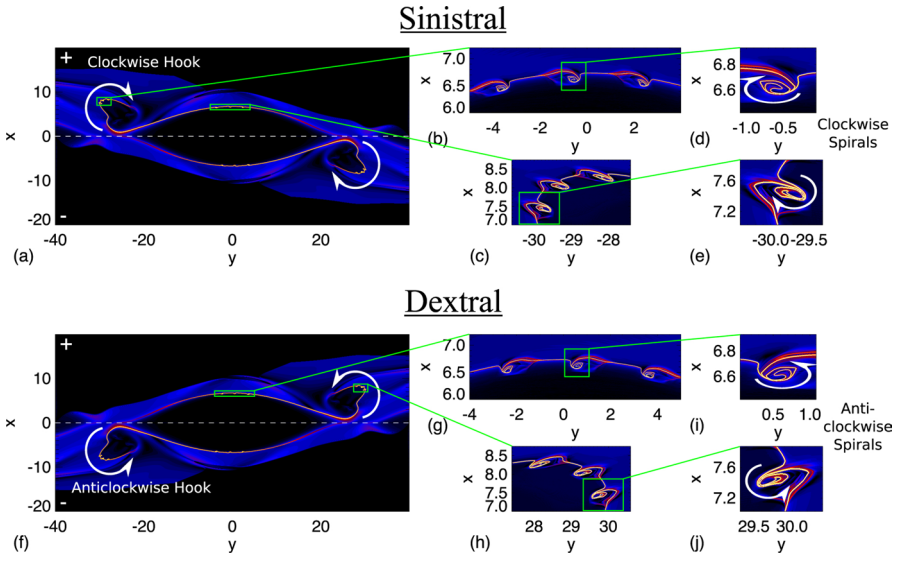

Fig. 17 Simulation results for fine structures in flare ribbons implementing tearing modes in the current sheet. The squashing factor map on the surface shows the shape of the flare ribbons and fine structure for sinistral (**a**) and dextral (**f**) flux ropes. Close-up views of the spirals within the green boxes in (**a**) are displayed in (**b–e**), and those in (**f**) are in (**g–j**). Arrows show the handedness of the hooks/spirals while the dashed line shows the PIL. Source: Wyper and Pontin (2021)

formed. The handedness of the spirals and waves must be the same as the handedness of the hooks of the main ribbon as indicated by the white circular arrows in Fig. 17a,f. They look qualitatively similar to the afore-mentioned solar flare ribbon observations. Notably, the anti-clockwise hook motion predicted for the dextral flux rope is similar to that of the observed Hα ribbon front at the end of the light bridge during the 2015-06-22T18:23 flare (Fig. 16). It therefore appears that solar flare ribbons present not only signatures of the large-scale magnetic variation, but potential evidence of the fragmented and turbulent nature of the reconnection current sheet.

6 Conclusion

We have discussed the physical nature of solar magnetic reconnection with emphasis on its dimensionality. In this effort, we have presented, as a guidance, simplified reconnection rates and energy conversion rates expressed in solar observables. In due course, dimensionality appears as the key factor. We then selected and confronted existing pieces of observational evidence with the 3D kinematic models in the MHD limit. This is complemented by selective topics in 2D reconnection along with nonstandard 2D behaviors. The main conclusion is that 3D magnetic structure and 3D reconnection physics are not generally the same. Although some reconnection processes in a complex 3D geometry can be decomposed into a combination of 2D reconnection processes, others cannot. Those involved with the rotational degree of freedom arising around a reconnection point represent a fully 3D reconnection process. Instead of summarizing each section, we contrast the issues raised in considering 3D versus 2D reconnection in solar flares.

1. Not every solar magnetic structure should produce 3D reconnection. For instance, an unsheared magnetic arcade and a symmetric fan-dome structure lack the magnetic field component parallel to the reconnection electric field needed for 3D reconnection. In these cases, 2D reconnection theory could adequately be used, as long as the magnetic field lines are not strongly sheared and inflow toward the reconnection point lies mostly in the same plane of magnetic fields.
2. Either a sheared arcade or a torsionally distorted fan dome is suitable for hosting 3D reconnection as the nonzero $\mathbf{E} \cdot \mathbf{B}$ condition is likely to be met. In this process, a rotational (derotational) motion arises around the reconnection point, in addition to the translational motion. This may be related to the fact that $\mathbf{E} \cdot \mathbf{B}$ is the source for magnetic helicity. Vibrational motions come in any dimension. Therefore the essential feature of 3D solar reconnection turns out to be the rotational degree of freedom, which is not yet fully cast into analytical formulations.
3. The frequently observed motions of brightness along ribbons have been considered irrelevant to the reconnection physics. This notion needs to be reconsidered in view of the slipping reconnection in PRFs (Aulanier et al. 2012; Dudík et al. 2014, 2016) and in CRFs (Masson et al. 2009; Reid et al. 2012). The present study adds torsional spine reconnection as another possible mechanism for solar

flares, in which case the parallel ribbon motion is not a secondary effect but the main driver.

4. In PRFs, the magnetic flux in one ribbon should match that in the other ribbon. In CRFs, the CR flux should be twice larger than the IR flux, which applies to both torsional and spine-fan reconnection. During spine-fan reconnection, the CR flux change associated with the outward shift from its original position should match that of the inwardly shifting CR, although both are in the same polarity.
5. In CRFs, a relative motion of CR and IR may result in a different orientation of the current built up around the 3D null point. If a CR rotates and no more flux is available beyond the CR, the current can develop in the direction of the spine ($N < 1$). If the IR rotates and the CR expands, the current develops in the fan direction ($N > 1$). Only one nominal direction of current layer is available in the 2D X-point reconnection, and $M < 1$ always. We found that N is related to the amount of magnetic twist.
6. The 3D null reconnection with current running parallel to the fan is known to have an analogy with 2D reconnection from the flux transfer viewpoint. However, even in this case, the analogy fails, because, unlike the expanding CR, the IR approaches the PIL, a 3D behavior opposite to that of the 2D reconnection. This distinction originates from the difference between the rotational flux transport around 3D null, and the translational flux transport toward the 2D X-point.
7. Both torsional waves traveling toward the 3D null and Alfvén waves toward the 2D X-point are hardly observable, but may be detectable through microwave polarization signatures. They seem to appear in the form of QPP driven by the rotational or vibrational motions of the line-tied fields, and more commonly be generated in a more or less symmetrical fan structure. In a system with less perfect symmetry, the torsional mode associated with currents parallel to either the spine or the fan tends to occur. Therefore, magnetic structure is the factor that determines which mode of reconnection is dominant around the 3D null point.
8. A couple of analogies between PRF and CRF reconnection are found. One is between the shear magnetic field component in PRFs and the torsional component in CRFs. Another is between CR's expanding motion and PR's separating motion. On the other hand, CR's contracting motion has no counterpart in PRF, i.e., approaching ribbon motion, because in the standard 2D X-configuration, the counter motion occurs in unobservable heights. In this sense, the configuration for the spine-fan reconnection might be regarded as a highly curved version of the X-configuration.
9. Extension of the 2D standard model to a 3D model may pursue two goals. One is to accommodate the motion along the ribbon axis to address its role in breaking the symmetry as in the strong-to-weak shear transition around a flare (Aulanier et al. 2012, 2013). The other is to explore what causes local acceleration of PRs (Cannon et al. 2022). The former can be addressed by including a time-dependent guide field, and the latter, by specifying complexity in a largescale magnetic structure.

10. Micro-physics introduced in the 2D standard model is essential in explaining fine structures within PRs. The variability in the PR area as well as its brightness could be explained in terms of pulsating current sheet under current instability. Fine structures in PRs such as wavelike perturbations and spirals could be explained in terms of tearing mode instability in the flare current sheet. It is therefore worthwhile to incorporate micro-physics into the 2D standard model if possible.

For future perspectives, we list several features, which are essential but not fully included in the present study:

1. How to couple the counter-rotational flow in torsional reconnection to the flux-transporting flow into the nonideal region is a non-trivial problem in theory (Hornig & Priest 2003). An empirical approach to determine their relationship using either solar observations or simulations of torsional Alfvén waves or helical jets during CRFs is warranted in this regard. As a related topic, we were able to relate the aspect ratio, N, of the torsionally nonideal region to an external driver, but size information of the nonideal region itself is needed for better understanding the physics of torsional reconnection.
2. Solar filaments that erupt due to an ideal or resistive MHD instability are likely to play an indispensable role as an external driver or trigger of the magnetic reconnection. Whilst such a filament eruption in PRFs naturally conforms to the 2D standard model (Fig. 1g), those in CRFs alter the fan-spine structure to invite more complicated scenarios of 3D reconnection. For instance, coexisting CRFs and PRFs may work together to produce a chain reaction of successive flares. Processes involving both ideal MHD and resistive MHD, although not full addressed in this study, certainly deserve further attention.
3. Thermal heating and nonthermal particle acceleration in the reconnection current sheet are important topics often developed apart from the MHD simulations. Lee et al. (2017, 2020a) studied thermal/nonthermal evolution of flares using the DEM analysis of EUV and X-ray emissions. Early rise of temperature and emission measure has implications on formation of a hot halo over the fan structure, and thus preconditioning reconnection and an eruption. Localized reconnection heating (Longcope et al. 2020) and chromospheric evaporation in CRFs (Zhang et al. 2016) are also interesting thermal processes that deserve further attention.
4. Microwave diagnostics on CRFs have not been utilized much to date. Nonthermal activation, a precursor of the breakout eruption, was also found in a microwave observation, which is too subtle to be detected in other thermal radiations. Mapping microwave polarization over a CRF provides a direct piece of magnetic polarity change around the null point. Quasi-periodic oscillations in microwave polarization lightcurves may prove the theoretical idea of the torsional null-point reconnection (Lee et al. 2020b; Lee 2022).
5. Last, but not least, is the finding that the large-scale magnetic connectivity may affect the local reconnection rate. This behavior is found when flare ribbons pass through a local region where magnetic connectivity rapidly changes. The

acceleration of the ribbon front in such regions implies that an increase in the reconnection rate depends on which coronal X-point is connected to the ribbon front at a given time. This is difficult to study with small-scale PIC simulations, but is important for solar physics.

Finally, we comment on the occurrence frequency of CRFs. 3D null reconnection in solar applications has attracted less attention in spite of its significance in reconnection theory. One drawback of 3D null reconnection is that CRFs occur only in a special configuration that is not commonly observed. Certainly, PRFs are more commonly found than CRFs perhaps due to the large number of bipolar active regions in the sun. Perfect CRFs may be rare but a fan-spine structure is found in a wide range of sizes, from small-scale embedded bipolar structures for small scales (Uritsky et al. 2021) to giant curtain like structures near large active regions for large scales (Liu et al. 2020). Also a group of active regions adjacent to a large-scale coronal hole can produce CMEs in a pseudo-streamer structure (Lim et al. 2017). Squashing factor maps (Titov et al. 2002) typically show many closed fan-like separatrices at these locations. This may be because many multipolarities exist to interact with each other. Their nested structure is potentially important for larger scale dynamics, which invites future challenges in the issue of energy conversion and the efficiency of reconnection for application in heliophysics and space weather.

Acknowledgements I thank anonymous reviewers for their careful reading of this manuscript and many critical comments. I thank Dr. David I. Pontin for providing his illustrations along with comments, which are used in a number of figures in this paper. I thank Dr. Gwangson Choe for insightful discussions, which helped finish this paper. I thank Dr. Chang Liu for his long-term collaborations with me, which motivated this study. This work was supported by NSF Grant AGS1954737 and NASA Grants 80NSSC21K1671 and 80NSSC21K0003.

Declarations

Conflict of interest The author claims that he has no conflicts of interest.

References

A.K. Al-Hachami, D.I. Pontin, Magnetic reconnection at 3D null points: effect of magnetic field asymmetry. A &A **512**, A84 (2010)

M.D. Altschuler, G. Newkirk, Magnetic fields and the structure of the solar corona, I: methods of calculating coronal fields. Sol. Phys. **9**, 131 (1969)
S.K. Antiochos, J.T. Karpen, C. R. DeVore, Coronal magnetic field relaxation by null-point. ApJ **575**, 578 (2002)
V. Archontis, F. Moreno-Insertis, K. Galsgaard, A. W. Hood, The three-dimensional interaction between emerging magnetic flux and a large-scale coronal field: reconnection, current sheets, and jets. ApJ **635**, 1299 (2005)
A. Asai, S. Masuda, T. Yokoyama et al., Difference between spatial distributions of the Hα kernels and hard X-ray sources in a solar flare. APJ **578**, L91 (2002)
A. Asai, T. Yokoyama, M. Shimojo, S. Masuda, H. Kurokawa et al., Flare ribbon expansion and energy release rate. ApJ **611**, 557–567 (2004)
G. Aulanier, E. Pariat, P. Démoulin, C.R. Devore, Slip-running reconnection in quasi-separatrix layers. Solar Phys. **238**, 347 (2006)
G. Aulanier, M. Janvier, B. Schmieder, The standard flare model in three dimensions. I. Strong-to-weak shear transition in post-flare loops. A &A **543A**, 110 (2012)
G. Aulanier, P. Démoulin, C.J. Schrijver et al., The standard flare model in three dimensions. II. Upper limit on solar flare energy. A &A **549A**, 66 (2013)
G. Baumann, T. Haugbølle, Å. Nordlund, Kinetic modeling of particle acceleration in a solar null-point reconnection region. ApJ **771**, 93 (2013)
M.A. Berger, Magnetic helicity in the solar corona. Dissertation: Ph. D. Harvard University (1984)
M.A. Berger, G.B. Field, The topological properties of magnetic helicity. J. Fluid Mech. **147**, 133 (1984)
J. Büchner, Locating current sheets in the solar corona. Sp. Sci. Rev. **122**, 149 (2006)
S.R. Brannon, D.W. Longcope, J. Qiu, Spectroscopic observations of an evolving flare ribbon substructure suggesting origin in current sheet waves. ApJ **810**, 4 (2015)
P.K. Browning, C. Gerrard, A.W. Hood et al., Simulations of energy release triggered by a kink instability, heating the corona by nanoflares. A &A **485**, 837 (2008)
B. Cannon, J. Jing, Q. Li, et al., Magnetic reconnection rate in the M6.5 solar flare on 2015 June 22. ApJ. (2022) **(submitted)**
H. Carmichael, The physics of solar flares, eds. Hess WN (NASA SP-50, Washington), p. 451 (1964)
X. Chen, Y. Yan, B. Tan et al., Quasi-periodic pulsations before and during a solar flare in AR 12242. ApJ **878**, 78 (2019)
X. Cheng, Q. Hao, M.D. Ding et al., A two-ribbon white-light flare associated with a failed solar eruption observed by ONSET, SDO, and IRIS. ApJ **809**, 46 (2015)
J. Dudík, M. Janvier, G. Aulanier et al., Slipping magnetic reconnection during an X-class solar flare observed by SDO/AIA. ApJ **784**, 144 (2014)
J. Dudík, V. Polito, M. Janvier et al., Slipping magnetic reconnection, chromospheric evaporation, implosion, and precursors in the 2014 September 10 X1.6-class solar flare. ApJ **823**, 41 (2016)
J.W. Dungey, The steady state of the Chapman-Ferraro problem in two dimensions. JGR **66**, 1043 (1961)
M. El-Batanouny, *Advanced Quantum Condensed Matter Physics* (Cambridge University Press, 2020)
L. Fletcher, J.A. Pollock, H.E. Potts, Tracking of TRACE ultraviolet flare footpoints. Solar Phys. **222**, 279 (2004)
T.G. Forbes, J. Lin, What can we learn about reconnection from coronal mass ejections? J. Atmos. Solar-Terr. Phys. **62**, 1499–1507 (2000)
T.G. Forbes, E.R. Priest, Reconnection in the solar atmosphere, in *Solar Terrestrial Physics: Present and Future*. ed. by D.M. Butler, K. Papadopoulos (NASA RP-1120, Washington DC, 1984), pp.1–35. (**1-39**)
R.J. French, S.A. Matthews, I. Jonathan Rae, A.W. Smith, Probing current sheet instabilities from flare ribbon dynamics. ApJ **922**, 117 (2021)
K. Galsgaard, A. Nordlund, Heating and activity of the solar corona. 3. Dynamics of a low beta plasma with three-dimensional null points. J. Geophys. Res. **102**, 231 (1997)
K. Galsgaard, D.I. Pontin, Steady state reconnection at a single 3D magnetic null point. A &A **529**, A20 (2011)
K. Galsgaard, E.R. Priest, V.S. Titov, Numerical experiments on wave propagation towards a 3D null point due to rotational motions. J. Geophys. Res. (Space Physics) **108**, 1042 (2003)
M. Goodbred, Y.-H. Liu, B. Chen, X. Li, The relation between the energy conversion rate and reconnection rate in Petschek-type reconnection-implications for solar flares. Phys. Plasmas **28**, 082103D (2021)
P.R. Goode, W. Cao, The 1.6 m off-axis new solar telescope (NST) in big bear. SPIE **8444**, E03 (2012)

P.C. Grigis, A.O. Benz, The evolution of reconnection along an arcade of magnetic loops. ApJ **625**, L143 (2005)
F. Guo, Y.-H. Liu, W. Daughton et al., Particle acceleration and plasma dynamics during magnetic reconnection in the magnetically dominated regime. ApJ **806**, 167 (2015)
F. Guo, X. Li, W. Daughton, Magnetic energy release, plasma dynamics, and particle acceleration in relativistic turbulent magnetic reconnection. ApJ **919**, 111 (2021)
M. Hesse, K. Schindler, A theoretical foundation of general magnetic reconnection. J. Geophys. Res. **93**, 5558 (1988)
T. Hirayama, Theoretical model of flares and prominences. I: evaporating flare model. Solar Phys. **34**, 323 (1974)
G. Hornig, An introduction to the geometry and topology of fluid flows, in *The Geometry of Reconnection*. ed. by R.L. Ricca (Kluwer, Dordrecht, 2001), pp.295–313
G. Hornig, Reconnection of magnetic fields, in *Fundamental Concepts*. ed. by J. Brin, E.R. Priest (Cambridge University Press, Cambridge, 2007), pp.25–45
G. Hornig, E.R. Priest, Evolution of magnetic flux in an isolated reconnection process. Phys. Plasmas **10**, 2712 (2003)
G. Hornig, K. Schindler, Magnetic topology and the problem of its invariant definition. Phys. Plasmas **3**, 781 (1996)
A.W. Hood, P.K. Browning, R.A.M. van der Linden, Coronal heating by magnetic reconnection in loops with zero net current. A &A **506**, 913 (2009)
Y. Hou, T. Li, S. Yang, J. Zhang, A secondary fan-spine magnetic structure in active region 11897. ApJ **871**, 4 (2019)
T.A. Howson, I. De Moortel, Magnetic reconnection and the Kelvin-Helmholtz instability in the solar corona. A &A **656A**, 112 (2021)
B.D. Hughes, Lattice dynamics, random walks, and nonintegral effective dimensionality. J. Math. Phys. **23**, 1688 (1982)
H. Isobe, H. Takasaki, K. Shibata, Measurement of the energy release rate and the reconnection rate in solar flares. ApJ **632**, 1184 (2005)
M. Janvier, G. Aulanier, E. Pariat et al., The standard flare model in three dimensions. III. Slip-running reconnection properties. A &A **555A**, 77 (2013)
M. Janvier, A. Savcheva, E. Pariat et al., Evolution of flare ribbons, electric currents, and quasiseparatrix layers during an X-class flare. A &A **591**, A141 (2016)
J.H. Jensen, Introducing fluid dynamics using dimensional analysis. Am. J. Phys. **81**, 688 (2013)
C. Jiang, S.T. Wu, X. Feng, Q. Hu, Formation and eruption of an active region sigmoid. I. A study by nonlinear force-free field modeling. ApJ **780**, 55 (2014)
C. Jiang, S.T. Wu, X. Feng, Q. Hu, Data-driven magnetohydrodynamic modelling of a flux-emerging active region leading to solar eruption. Nat. Commun. **7**, 11522 (2016)
J. Jing, J. Lee, C. Liu, D.E. Gary, H. Wang, Hard X-ray intensity distribution along Hα ribbons. ApJ **664**, L127 (2007)
J. Jing, Y. Xu, W. Cao et al., Unprecedented fine structure of a solar flare revealed by the 1.6 m new solar telescope. NatSR **6**, 24319 (2016)
N.C. Joshi, C. Liu, X. Sun, H. Wang, T. Magara, Y.-J. Moon, The role of erupting sigmoid in triggering a flare with parallel and large-scale quasi-circular ribbons. ApJ **812**, 50 (2015)
N.C. Joshi, B. Joshi, P.K. Mitra, Evolutionary stages and triggering process of a complex eruptive flare with circular and parallel ribbons. MNRAS **501**, 4703 (2021)
R.A. Kopp, G.W. Pneuman, Magnetic reconnection in the corona and the loop prominence phenomenon. SoPh **50**, 85 (1976)
B. Kliem, T. Török, Torus instability. Phys. Rev. Lett. **96**, 255002 (2006)
B. Kliem, M. Karlický, A.O. Benz, Solar flare radio pulsations as a signature of dynamic magnetic reconnection. A &A **360**, 715 (2000)
B. Kliem, V.S. Titov, T. Török, Formation of current sheets and sigmoidal structure by the Kink instability of a magnetic loop. A &A **413**, L23 (2004)
D. Kuridze, M. Mathioudakis, A.F. Kowalski, Failed filament eruption inside a coronal mass ejection in active region 11121. A &A **552**, A55 (2013)
J. Lee, Radio emissions from solar active regions. Sp. Sci. Rev. **133**, 73 (2007)
J. Lee, Microwave perspective on magnetic breakout eruption. Front. Astron. Sp. Sci. **9**, 855737 (2022)
J. Lee, D.E. Gary, Parallel motions of coronal hard X-ray source and Hα ribbons. ApJ **685L**, 87 (2008)

J. Lee, S.M. White, M.R. Kundu et al., Microwave mode coupling above active regions as a coronal density diagnostic. SoPh **180**, 193 (1998)
J. Lee, D.E. Gary, G.S. Choe, Magnetic energy release during the 2002 September 9 solar flare. ApJ **647**, 638 (2006)
J. Lee, C. Liu, J. Jing et al., Solar eruption and local magnetic parameters. ApJ **831L**, 18 (2016a)
J. Lee, C. Liu, J. Jing et al., Solar multiple eruptions from a confined magnetic structure. ApJ **829L**, 1 (2016b)
J. Lee, S.M. White, J. Jing et al., Thermal and nonthermal emissions of a composite flare derived from NoRH and SDO observations. ApJ **850**, 124 (2017)
J. Lee, S.M. White, C. Liu et al., Magnetic structure of a composite solar microwave burst. ApJ **856**, 70 (2018)
J. Lee, J.T. Karpen, C. Liu et al., Heating and eruption of a solar circular ribbon flare. ApJ **893**, 158 (2020a)
J. Lee, S.M. White, X. Chen et al., Microwave study of a solar circular ribbon flare. ApJ **901**, L10 (2020b)
T. Li, J. Zhang, Quasi-periodic slipping magnetic reconnection during an X-class solar flare observed by the solar dynamics observatory and interface region imaging spectrograph. ApJ **804L**, 8 (2015)
T. Li, Y. Hou, S. Yang, J. Zhang, Three-dimensional magnetic reconnection triggering an X-class confined flare in active region 12192. ApJ **869**, 172 (2018a)
T. Li, S. Yang, Q. Zhang, Y. Hou, J. Zhang, Two episodes of magnetic reconnections during a confined circular-ribbon flare. ApJ **859**, 122 (2018b)
X. Li, J. Zhang, S. Yang, Y. Hou, R. Erdélyi, Observing Kelvin-Helmholtz instability in solar blowout jet. NatSR **8**, 8136 (2018c)
T. Li, L. Liu, Y. Hou, J. Zhang, Two types of confined solar flares. ApJ **881**, 151 (2019)
T. Li, E. Priest, R. Guo, Three-dimensional magnetic reconnection in astrophysical plasmas. Proc. R. Soc. A. **477**, 20200949 (2021)
E.-K. Lim, V. Yurchyshyn, P. Kumar, Observation of a large-scale quasi-circular secondary ribbon associated with successive flares and a halo CME. ApJ **850**, 167 (2017)
C. Liu, J. Lee, D.E. Gary, H. Wang, The ribbon-like hard X-ray emission in a sigmoidal solar active region. ApJ **658L**, 127 (2007)
C. Liu, J. Lee, J. Jing et al., The spatial distribution of the hard X-ray spectral index and the local magnetic reconnection rate. ApJ **672L**, 69 (2008)
C. Liu, N. Deng, J. Lee, et al., Three-dimensional magnetic restructuring in two homologous solar flares in the seismically active NOAA AR 11283. ApJ **795**, 128 (2014)
C. Liu, J. Lee, H. Wang, The eruption of outer spine-like loops leading to a double-stage circular-ribbon flare. ApJ **883**, 47 (2019)
C. Liu, A. Prasad, J. Lee et al., An eruptive circular-ribbon flare with extended remote brightenings. ApJ **899**, 34 (2020)
D. Longcope, Solar flares. Oxf. Res. Encycl. Phys. (2020). https://doi.org/10.1093/acrefore/9780190871994.013.20
D. Longcope, M. McCarthy, A. Malanushenko, Localized reconnection heating inferred from the three-dimensional locations of bright active region coronal loops. ApJ **901**, 147 (2020)
C.H. Mandrini, B. Schmieder, P. Démoulin et al., Topological analysis of emerging bipole clusters producing violent solar events. Sol. Phys. **289**, 2041 (2014)
S. Masson, E. Pariat, G. Aulanier, C.J. Schrijver, The nature of flare ribbons in coronal null-point topology. ApJ **700**, 559 (2009)
S. Masson, E. Pariat, G. Valori, N. Deng, C. Liu, H. Wang, H. Reid, Flux rope, hyperbolic flux tube, and late extreme ultraviolet phases in a non-eruptive circular-ribbon flare. A &A **604**, A76 (2017)
J.A. McLaughlin, A.W. Hood, I. de Moortel, Review article: MHD wave propagation near coronal null points of magnetic fields. Space Sci. Rev. **158**, 205 (2011)
S.K. Mishra, B. Singh, A.K. Srivastava, Evolution of Kelvin-Helmholtz instability in the fan-spine topology. ApJ **923**, 72 (2021)
S.J. Naus, J. Qiu, C.R. DeVore, S.K. Antiochos, Correlated spatio-temporal evolution of EUV ribbons and hard X-rays in a solar flare. ApJ **926**, 218 (2022)
W.A. Newcomb, Motion of magnetic lines of force. Ann. Phys. **3**, 347 (1958)
L. Ofman, B.J. Thompson, SDO/AIA observation of Kelvin-Helmholtz instability in the solar corona. ApJ **734L**, 11 (2011)
R. Pallister, P.F. Wyper, D.I. Pontin et al., Spatially separated electron and proton beams in a simulated solar coronal jet. ApJ **923**, 163 (2021)

E. Pariat, S.K. Antiochos, C.R. DeVore, A model for solar polar jets. ApJ **691**, 61 (2009)
E. Pariat, S.K. Antiochos, C.R. DeVore, Three-dimensional modeling of quasi-homologous solar jets. ApJ **714**, 1762 (2010)
E. Pariat, K. Dalmasse, C.R. DeVore et al., Model for straight and helical solar jets. I. Parametric studies of the magnetic field geometry. A &A **573**, A130 (2015)
E.N. Parker, Sweet's mechanism for merging magnetic fields in conducting fluids. J. Geophys. Res. **62**, 509 (1957)
J. Parker, D. Longcope, Modeling a propagating sawtooth flare ribbon structure as a tearing mode in the presence of velocity shear. ApJ **847**, 30 (2017)
G. Paschmann, M. Øieroset, T. Phan, In-situ observations of reconnection in space. Sp. Sci. Rev. **178**, 385 (2013)
H.E. Petschek, Magnetic reconnection, in *The Physics of Solar Flares*. ed. by W.N. Hess (NASA SP-50, Washington DC, 1964), pp.425–439
D.I. Pontin, Three-dimensional magnetic reconnection regimes: a review. Adv. Sp. Res. **47**, 1508 (2011)
D.I. Pontin, Theory of magnetic reconnection in solar and astrophysical plasmas. Phil. Trans. R. Soc. A **370**, 3169 (2012)
D.I. Pontin, K. Galsgaard, Current amplification and magnetic reconnection at a three-dimensional null point: physical characteristics. J. Geophys. Res. **112**, A03103 (2007)
D.I. Pontin, E.R. Priest, Magnetic reconnection: MHD theory and modelling. Liv. Rev. Solar Phys. **19**, 1 (2020)
D.I. Pontin, G. Hornig, E.R. Priest, Kinematic reconnection at a magnetic null point: spine-aligned current. Geophys. Astrophys. Fluid Dyn. **98**, 407 (2004)
D.I. Pontin, K. Galsgaard, G. Hornig, E.R. Priest, A fully magnetohydrodynamic simulation of 3D non-null reconnection. Phys. Plasmas **12**, 052307 (2005a)
D.I. Pontin, G. Hornig, E.R. Priest, Kinematic reconnection at a magnetic null point: fan-aligned current. Geophys. Astrophys. Fluid Dyn. **99**, 77 (2005b)
D.I. Pontin, E.R. Priest, K. Galsgaard, On the nature of reconnection at a solar coronal null point above a separatrix dome. ApJ **774**, 154 (2013)
D.I. Pontin, K. Galsgaard, P. Démoulin, Why are flare ribbons associated with the spines of magnetic null points generically elongated? SoPh **291**, 1739 (2016)
E.R. Priest, *Magnetohydrodynamics of the Sun* (Cambridge University Press, Cambridge, 2014)
E.R. Priest, T.G. Forbes, *Magnetic Reconnection: MHD Theory and Applications* (Cambridge University Press, Cambridge, 2000)
E.R. Priest, D.I. Pontin, Three-dimensional null point reconnection regimes. Phys. Plasmas **16**, 122101 (2009)
E.R. Priest, V.S. Titov, Magnetic reconnection at three-dimensional null points. Phil. Trans. R. Soc. A **354**, 2951 (1996)
E.R. Priest, G. Hornig, D.I. Pontin, On the nature of three-dimensional magnetic reconnection. J. Geophys. Res. **108**, 1285 (2003)
J. Qiu, J. Lee, D.E. Gary et al., Motion of flare footpoint emission and inferred electric field in reconnecting current sheets. ApJ **565**, 1335 (2002)
H.A.S. Reid, N. Vilmer, G. Aulanier et al., X-ray and ultraviolet investigation into the magnetic connectivity of a solar flare. A &A **547**, A52 (2012)
G.J. Rickard, V.S. Titov, Current accumulation at a three-dimensional magnetic null. ApJ **472**, 840 (1996)
K.H. Schatten, J.M. Wilcox, N.F. Ness, A model of interplanetary and coronal magnetic fields. Sol. Phys. **6**, 442 (1969)
K. Schindler, M. Hesse, J. Birn, General magnetic reconnection, parallel electric fields, and helicity. JGR **93**, 5547 (1988)
K. Shibata, S. Tanuma, Plasmoid-induced-reconnection and fractal reconnection. Earth Planets Sp. **53**, 473 (2001). https://doi.org/10.1186/BF03353258
P.A. Sturrock, A model of solar flares. In: Structure and Development of Solar Active Regions, Budapest, Hungary, 4–8 Sep (1967)
X. Sun, J.T. Hoeksema, Y. Liu et al., Hot spine loops and the nature of a late-phase solar flare. ApJ **778**, 139 (2013)
P.A. Sweet, *Electromagnetic Phenomena in Cosmical Physics* (Cambridge University Press, New York, 1958)
V.S. Titov, G. Hornig, P. Démoulin, Theory of magnetic connectivity in the solar corona. JGRA **107**, 1164 (2002)

S. Toriumi, Y. Katsukawa, M.C.M. Cheung, Light bridge in a developing active region. I. Observation of light bridge and its dynamic activity phenomena. ApJ **811**, 137 (2015)
V.M. Uritsky, C.E. DeForest, J.T. Karpen et al., Plumelets: dynamic filamentary structures in solar coronal plumes. ApJ **907**, 1 (2021)
H. Wang, C. Liu, Circular ribbon flares and homologous jets. ApJ **760**, 101 (2012)
T. Wiegelmann, Optimization code with weighting function for the reconstruction of coronal magnetic fields. SoPh **219**, 87 (2004)
P.F. Wyper, R. Jain, The effects of localizing the non-ideal term, torsional magnetic reconnection. JPlPh **77**, 843 (2011)
P.F. Wyper, D.I. Pontin, Is flare ribbon fine structure related to tearing in the flare current sheet? ApJ **920**, 102 (2021)
P.F. Wyper, S.K. Antiochos, C.R. DeVore, A universal model for solar eruptions. Nature **544**, 452 (2017)
M. Yamada, J. Yoo, J. Jara-Almonte, H. Ji, R.M. Kulsrud et al., Conversion of magnetic energy in the magnetic reconnection layer of a laboratory plasma. Nat. Commun. **5**, 4774 (2004)
M. Yan, L.C. Lee, E.R. Priest, Fast magnetic reconnection with small shock angles. J. Geophys. Res. **97**, 8277 (1992)
T. Yokoyama, K. Akita, T. Morimoto et al., Clear evidence of reconnection inflow of a solar flare. ApJ. **546L**, 69 (2001)
H. Zirin, *The Astrophysics of the Sun* (Cambridge University Press, 1988)
Q.M. Zhang, Z.J. Ning, Y. Guo et al., Multiwavelength observations of a partially eruptive filament on 2011 September 8. ApJ **805**, 4 (2015)
Q.M. Zhang, D. Li, Z.J. Ning et al., Explosive chromospheric evaporation in a circular-ribbon flare. ApJ **827**, 27 (2016)
Q. Zhang, F. Guo, W. Daughton et al., Efficient nonthermal ion and electron acceleration enabled by the flux-rope Kink instability in 3D nonrelativistic magnetic reconnection. PhRvL **127r**, 5101 (2021)
J. Zhao, S.A. Gilchrist, G. Aulanier et al., Hooked flare ribbons and flux-rope-related QSL footprints. ApJ **823**, 62 (2016)
Z. Zhong, Y. Guo, M. Ding, C. Fang, Q. Hao, Transition from circular-ribbon to parallel-ribbon flares associated with a bifurcated magnetic flux rope. ApJ **871**, 105 (2019)